



A Complete 16 μm Selected Galaxy Sample at $z \sim 1$: Mid-infrared Spectral Energy Distributions

J.-S. Huang^{1,2}, Y.-S. Dai (戴昱)^{1,15}, S. P. Willner³, S. M. Faber⁴, C. Cheng¹, H. Xu¹, H. Yan⁵, S. Wu¹, X. Shao¹, C. Hao⁶, X. Xia⁶, D. Rigopoulou⁷, M. Pereira Santaella^{7,8}, G. Magdis^{9,10,11}, I. Cortzen⁹, G. G. Fazio³, P. Assmann¹², L. Fan^{13,14}, M. Musin¹, Z. Wang¹, K. C. Xu¹, C. He¹, G. Jin¹, and A. Esamdin¹⁴

¹ National Astronomical Observatories, Chinese Academy of Sciences, Beijing 100012, People's Republic of China; ydai@nao.cas.cn

² CAS Key Laboratory of Optical Astronomy, National Astronomical Observatories, Chinese Academy of Sciences, Beijing 100101, People's Republic of China

³ Center for Astrophysics, Harvard & Smithsonian| Cambridge, MA 02138, USA

⁴ University of California Observatories/Lick Observatory, University of California, Santa Cruz, CA 95064, USA

⁵ Department of Physics and Astronomy, University of Missouri-Columbia, MO, USA

⁶ Tianjin Astrophysics Center, Tianjin Normal University, Tianjin 300387, People's Republic of China

⁷ Department of Astrophysics, Oxford University, Keble Road, Oxford, OX1 3RH, UK

⁸ Centro de Astrobiología (CSIC-INTA), Ctra. de Ajalvir, km 4, E-28850, Torrejón de Ardoz, Madrid, Spain

⁹ Cosmic Dawn Center (DAWN), Copenhagen, Denmark

¹⁰ DTU-Space, Technical University of Denmark, Elektrovej 327, DK-2800 Kgs. Lyngby, Denmark

¹¹ University of Copenhagen, Lyngbyvej 2, DK-2100 Copenhagen Ø, Denmark

¹² Department of Astronomy, University of Concepcion, Concepcion, Chile

¹³ CAS Key Laboratory for Research in Galaxies and Cosmology, Department of Astronomy, University of Science and Technology of China, Hefei 230026, People's Republic of China

¹⁴ School of Astronomy and Space Sciences, University of Science and Technology of China, Hefei, Anhui 230026, People's Republic of China

Received 2020 May 29; revised 2021 February 10; accepted 2021 March 3; published 2021 May 28

Abstract

We describe a complete, flux-density-limited sample of galaxies at redshift $0.8 < z < 1.3$ selected at 16 μm . At the selection wavelength near 8 μm rest, the observed emission comes from both dust heated by intense star formation and active galactic nuclei (AGNs). Fitting the spectral energy distributions (SEDs) of the sample galaxies to local-galaxy templates reveals that more than half the galaxies have SEDs dominated by star formation. About one-sixth of the galaxy SEDs are dominated by an AGN, and nearly all of the rest of the SEDs are composite. Comparison with X-ray and far-infrared observations shows that combinations of luminosities at rest-frame 4.5 and 8 μm give good measures of both AGN luminosity and star formation rate. The sample galaxies mostly follow the established star-forming main sequence for $z = 1$ galaxies, but of the galaxies more than 0.5 dex above that main sequence, more than half have AGN-type SEDs. Similarly, the most luminous AGNs tend to have higher star formation rates than the main-sequence value. Galaxies with stellar masses $> 10^{11} M_{\odot}$ are unlikely to host an AGN. About 1% of the sample galaxies show an SED with dust emission typical of neither star formation nor an AGN.

Unified Astronomy Thesaurus concepts: [Infrared galaxies \(790\)](#); [Luminous infrared galaxies \(946\)](#); [Sky surveys \(1464\)](#); [Spectral energy distribution \(2129\)](#)

1. Introduction

Star formation rate (SFR), stellar mass, and growth of central supermassive black holes (SMBHs) are critical factors in regulating mass assembly in galaxies. Star formation occurring in galaxies can be classified into three phases (e.g., Daddi et al. 2010; Elbaz et al. 2011): a main sequence in which SFR and stellar mass for most galaxies have a redshift-dependent correlation with roughly a factor of 3 (but varying with stellar mass) dispersion (Davies et al. 2019), a starburst phase in which galaxies have an SFR more than a factor of 3 above the main-sequence relation (Elbaz et al. 2018), and a quiescent phase with SFR more than a factor of 3 below the main-sequence relation.

Rapid cessation of star formation (“quenching”) is required for massive galaxies to limit their numbers to those observed in the local universe (Huang et al. 2003, 2013; Faber et al. 2007). Several proposed mechanisms to quench star formation involve galaxies’ central SMBHs. SMBH masses are linearly proportional to masses of their hosting bulge (Kormendy & Richstone 1995; Magorrian et al. 1998), and therefore, every galaxy bulge is presumed to contain an SMBH. The SMBH

must grow along with its host bulge to maintain the observed linearity (Netzer 2009; Rigopoulou et al. 2009; Rosario et al. 2013; Lapi et al. 2014; Lanzuisi et al. 2017). Indeed, many observations have found a correlation between the active galactic nucleus (AGN) accretion luminosity and host-galaxy SFR (Hao et al. 2005a, 2008; Silverman et al. 2008; Madau & Dickinson 2014; Dai et al. 2018).

A galaxy’s spectral energy distribution (SED) in the rest-frame near- and mid-infrared (NIR and MIR: 1–30 μm) contains rich information about stellar mass, star formation, and AGN activity. To estimate galaxy stellar masses, photometry at rest wavelength $\lambda \sim 600$ nm can be used, but NIR is better (Bell et al. 2003; Huang et al. 2013; McGaugh & Schombert 2014). Wavelengths much shorter than 600 nm are not good because they are emitted only by hotter stars that make up only a small fraction of the mass. Because stellar emission from galaxies at $z > 1$ is shifted to the observed NIR for rest-frame 600 nm and to MIR for rest-frame NIR, estimating stellar mass with only observed visible photometry becomes impossible. After the Spitzer Space Telescope was launched in 2003, IRAC 3.6–8 μm photometry became the benchmark for measuring the stellar mass of high-redshift galaxies (Rigopoulou et al. 2009; Magdis et al. 2010b; Huang et al. 2013).

¹⁵ Corresponding author.

Despite the complexity of galaxy SEDs, photometry at rest-frame MIR wavelengths is often used to estimate SFRs. Based on a local star-forming galaxy sample, Calzetti et al. (2007) argued that rest-frame $24\ \mu\text{m}$ emission arises from hot dust heated directly by OB stars in star formation regions, and therefore, $24\ \mu\text{m}$ luminosities in these galaxies are linearly correlated with SFR. Chary & Elbaz (2001), Alonso-Herrero et al. (2006), Calzetti et al. (2007), and Rieke et al. (2009) used local star-forming galaxy samples to establish such a linear conversion and proposed that it can apply to galaxies at high redshift with a correct set of templates. However, estimating SFR for galaxies at high redshift using their *observed* $24\ \mu\text{m}$ flux densities requires an accurate K -correction. At $1 < z < 3$, the MIPS $24\ \mu\text{m}$ band samples rest-frame $6\ \mu\text{m} < \lambda < 12\ \mu\text{m}$, where there are strong spectral features such as the polycyclic aromatic hydrocarbon (PAH) emission features at 6.2 , 7.7 , and $8.6\ \mu\text{m}$ and the silicate absorption at $10\ \mu\text{m}$. Some dusty galaxies at $z \sim 1.4$ have such a deep silicate absorption that they have no $24\ \mu\text{m}$ detection even in the deepest MIPS image but are clearly detected at longer wavelengths (Magdis et al. 2010a). Therefore, the MIPS $24\ \mu\text{m}$ K -correction for galaxies in this redshift range can vary substantially and is very sensitive to both redshift and the SED. A $24\ \mu\text{m}$ selected sample may therefore yield a diverse galaxy population.

The rest-frame $8\ \mu\text{m}$ luminosity L_8 is also considered a tracer of SFR (e.g., Wu et al. 2005; Mahajan et al. 2019). Broadband photometry at this (rest) wavelength measures mainly PAH emission features at 7.7 and $8.6\ \mu\text{m}$, perhaps with some contribution from the $6.2\ \mu\text{m}$ feature (Pahre et al. 2004). More recently, Cortzen et al. (2019) found that the PAH emission correlates with cold molecular gas in star-forming galaxies but that should not be a problem because molecular gas will be correlated with the SFR in most galaxies. Even so, PAH emission may not trace star formation: (1) in H II regions, where PAH molecules can be destroyed by the strong UV radiation field (Helou et al. 2001; Houck et al. 2004; Pety et al. 2005); (2) where sources unrelated to star formation, such as evolved stars and diffuse light, excite PAH (Li & Draine 2002; Boselli et al. 2004; Peeters et al. 2004); and (3) in galaxies with low metallicity (Engelbracht et al. 2005; Galliano et al. 2005; Hogg et al. 2005; Rosenberg et al. 2006; G. Jin et al. 2021, in preparation). G. Jin et al. (2021, in preparation) found that the ratio of $8\ \mu\text{m}$ luminosity to SFR remains constant for galaxies with $M_* > 10^9 M_\odot$ but decreases rapidly with metallicity for galaxies with $M_* < 10^9 M_\odot$. Despite the potential complications, Elbaz et al. (2011) found that rest-frame $8\ \mu\text{m}$ luminosity L_8 has a good linear correlation with L_{IR} with $\langle L_{\text{IR}}/L_8 \rangle \sim 5$ for galaxies at $0 < z < 2$, and Mahajan et al. (2019) found L_8 to be a good SFR measure for most local star-forming galaxies. Because L_8 is such a good star formation tracer, many studies have used MIPS $24\ \mu\text{m}$ surveys to select star-forming galaxies at $z \sim 2$ (Huang et al. 2007, 2009; Farrah et al. 2008; Desai et al. 2009; Fang et al. 2014).

AGN emission is another uncertain factor adding to the already-complicated galaxy MIR SEDs. A bare AGN typically shows a $\nu F_\nu \approx \text{constant}$ SED in the MIR (Ward et al. 1987), much redder than starlight. Some Palomar-Green (PG) quasars even display a silicate emission feature from the inner side of their dusty torus (Hao et al. 2005b). Any AGN emission shows up in the IRAC bands (Lacy et al. 2004; Stern et al. 2005; Alonso-Herrero et al. 2006) and is often the dominant MIR component. When the AGN component is dominant, it is

proportional to X-ray luminosity (Carleton et al. 1987; Lutz et al. 2004; Lanzuisi et al. 2009; Stern 2015). If an AGN component is neglected, the SFR derived from the rest-frame $8\ \mu\text{m}$ luminosity or observed $24\ \mu\text{m}$ flux density will be overestimated. For galaxies with overwhelming AGN emission, MIR photometry does not measure SFR at all.

This paper presents an SED study of a complete $16\ \mu\text{m}$ selected galaxy sample at $0.8 < z < 1.3$. It is part of a series studying rest-frame $8\ \mu\text{m}$ selected galaxies at $z = 0.3$, 1 , and 1.9 via the observed bands of IRAC $8\ \mu\text{m}$, IRS peakup/Akari $\sim 16\ \mu\text{m}$, and MIPS $24\ \mu\text{m}$ (Huang et al. 2007, 2009; Fang et al. 2014; G. Jin et al. 2021, in preparation). At $z \sim 1$, the PAH emission features at 6.2 , 7.7 , and $8.6\ \mu\text{m}$ are shifted into the observed $16\ \mu\text{m}$ band. The sample will therefore contain many star-forming galaxies, but also strong AGNs. Fitting the galaxy SEDs with a set of local templates reveals the demography of this sample and identifies the AGNs. A well-determined SED also permits accurate measurement of monochromatic luminosities $L_{4.5}$ and L_8 , thus giving an estimate of AGN luminosity and SFR. The $16\ \mu\text{m}$ sample is from the well-studied extragalactic fields Extended Groth Strip (EGS), GOODS-South (GOODS-S), and GOODS-North (GOODS-N), providing a high rate of spectroscopic redshifts. When spectroscopic redshifts are not available, we use photometric redshifts, which are reliable in these fields (Dahlen et al. 2013; Huang et al. 2013). In the GOODS fields, our galaxy sample is complete to $L_8 = 7.7 \times 10^9 L_\odot$ at $z = 1$, corresponding to $\text{SFR} = 3 M_\odot \text{yr}^{-1}$.

The structure of this paper is as follows: Section 2 describes the sample. Section 3 presents the MIR SEDs of star-forming galaxies and AGNs in the sample. Section 4 gives SFR estimates and establishes the SFR–stellar-mass and SFR–AGN luminosity relations for the sample. Section 5 is a brief summary. Throughout the paper, we adopt the Chabrier (2003) initial mass function. Source distances are based on a standard flat Λ CDM cosmology with $H_0 = 70\ \text{km s}^{-1} \text{Mpc}^{-1}$ and $\Omega_M = 0.30$.

2. The $16\ \mu\text{m}$ Selected Sample

We chose a $16\ \mu\text{m}$ selected sample for galaxies at $z \sim 1$ to include the strong PAH emission features. The earliest surveys were by the Infrared Space Observatory (ISO; Elbaz et al. 1999; Gruppioni et al. 2002; Rodighiero et al. 2004) at $15\ \mu\text{m}$. Larger and deeper surveys came from Akari/IRC at $15\ \mu\text{m}$ and the Spitzer/IRS peakup imager at $16\ \mu\text{m}$ (Wada et al. 2007; Burgarella et al. 2009; Pearson et al. 2010; Teplitz et al. 2011). The present study uses photometric catalogs from the latter two surveys. Figure 1 shows that the Spitzer/IRS and Akari/IRC bandpasses have similar profiles. Teplitz et al. (2011) compared the flux densities for GOODS-S objects detected by both instruments and found an average 1.3 times higher flux density measured by Spitzer/IRS at $16\ \mu\text{m}$ than by Akari/IRC at $15\ \mu\text{m}$. We have scaled the Akari photometry accordingly to its IRS $16\ \mu\text{m}$ equivalent.

Our $16\ \mu\text{m}$ sample¹⁶ has flux density limits $f_{16} > 30\ \mu\text{Jy}$ in GOODS-N/S and $f_{15} > 100\ \mu\text{Jy}$ (corresponding to $f_{16} > 130\ \mu\text{Jy}$) in the EGS, the respective detection limits. All three fields have extensive redshift surveys, and all $16\ \mu\text{m}$ sources above our selection limits have redshifts available, either

¹⁶ Hereafter, a $16\ \mu\text{m}$ selected sample refers to the galaxy sample selected from either Akari $15\ \mu\text{m}$ or Spitzer/IRS peakup $16\ \mu\text{m}$ photometric catalogs.

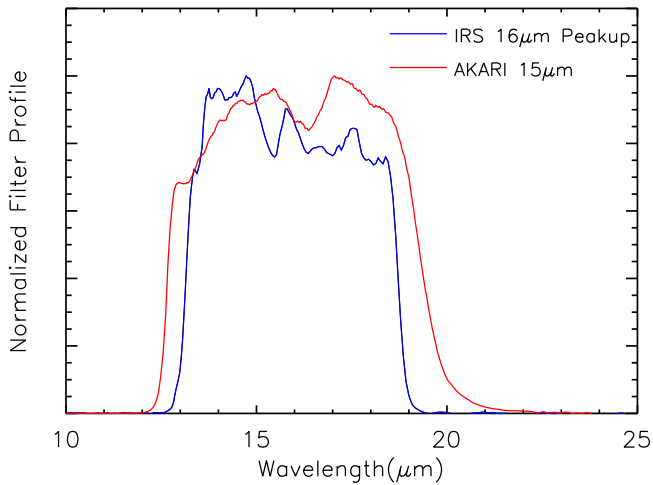


Figure 1. Normalized filter transmission profiles. The red line shows the Akari/IRC 15 μm profile, and the blue line shows the Spitzer/IRS 16 μm peakup imager profile. The Akari 15 μm filter profile in general overlaps with but is slightly wider than the IRS 16 μm profile.

spectroscopic or photometric. Our final sample comprises sources with $0.8 < z < 1.3$. This includes 556 objects based on spectroscopic redshifts and 149 objects based on photometric redshifts. Table 1 summarizes the sample characteristics.

Accurate redshifts are crucial for understanding the properties of sample galaxies. MIR galaxy spectra can include strong PAH emission and silicate absorption features. Redshift uncertainties will therefore cause substantial uncertainties in the K -correction to convert observed 16 μm flux densities (f_{16}) to rest-frame 8 μm luminosities L_8 for galaxies at $z \sim 1$. As noted above, 79% of the sample galaxies have spectroscopic redshifts. The extensive multi-band photometry in our survey fields also gives excellent photometric redshift measurements with $\Delta z/(1+z) \sim 0.03$ (Dahlen et al. 2013; Huang et al. 2013). This gives K -corrections adequate to within several percent, depending on the exact redshift and SED of individual sources.

Multiwavelength photometry is required for this project. We need photometry in all four IRAC bands as well as MIPS 24 μm for the SED fitting and classification. The three fields have deep Spitzer/IRAC and MIPS coverage, and every 16 μm object was detected in all four IRAC bands and in the MIPS 24 μm band. There are also rich HST and ground-based visible/NIR data available in these fields (Huang et al. 2013; Fang et al. 2018). We utilized the derived stellar mass M_* and SFR from CANDELS (Fang et al. 2018) when available. For EGS galaxies outside the CANDELS area, M_* and SFR came from Huang et al. (2013). (See Section 4.3 for more on the mass determination.) Figure 2 shows that most galaxies in this sample have rest $U - V$ colors bluer than the red sequence but at or near the red edge of the blue cloud, i.e., they are in the “green valley.” The stellar masses for this sample are in the range of $9.5 < \log_{10}(M_*/M_\odot) < 11.5$ with a mean of $\langle \log(M_*/M_\odot) \rangle = 10.3$.

All three fields have deep MIPS 70 μm ¹⁷ and Herschel/PACS and SPIRE data. The GOODS fields have limiting flux densities of 2.5 mJy at 70 μm , 1–3 mJy in the PACS bands, and ~ 10 mJy in the SPIRE bands. Those sufficed to detect 70%–80% of the sample in at least one Herschel band

(Elbaz et al. 2011). The EGS field has limiting flux densities of 2.5 mJy at 70 μm , 10 mJy in the PACS bands, and 14–16 mJy in the SPIRE bands. With this shallower Herschel coverage, only 40% of the sample was detected (Lutz et al. 2011; Oliver et al. 2012). We calculated L_{IR}^{H} for the sample with two methods (Elbaz et al. 2011): (A) convert 24 μm flux densities based on the best-fit template from Chary & Elbaz (2001) to give $L_{\text{IR}}^{\text{CE}}$, and (B) integrate the SED given by Herschel and MIPS 70 μm flux densities to give L_{IR}^{H} . Because every object in the sample was 24 μm detected, we were able to estimate $L_{\text{IR}}^{\text{CE}}$ for all objects in the sample, but only objects with FIR photometry in at least 2 bands permit estimates of L_{IR}^{H} . For our sample, $L_{\text{IR}}^{\text{CE}}$ are generally consistent with L_{IR}^{H} with scatter 0.18 dex.

The different sample-selection depths in EGS and GOODS yield slightly different demographics in luminosity classes. In the two GOODS fields, 72% of objects are LIRGs, and only 2% are ULIRGs. In the shallower EGS, 85% are LIRGs, and 6% are ULIRGs. Altogether, our sample is more than 70% LIRGs, a dominant population for the star formation rate density (SFRD) at $z \sim 1$ (Le Floch et al. 2005).

AGN emission can make a significant contribution to galaxy SEDs in the MIR (Dai et al. 2014), and therefore, it is important to measure the AGN contribution. In principle, almost all massive galaxies harbor an AGN of different stages. X-ray data can identify at least some AGNs, and deep X-ray surveys from Chandra already exist in our three fields. Depths are 800 ks in the EGS (Nandra et al. 2015), 2 Ms in GOODS-N (Xue et al. 2016), and 7 Ms in GOODS-S (Luo et al. 2017). These depths detected 24 Chandra X-ray sources in the EGS, 59 in GOODS-N, and 46 in GOODS-S. Only 10 sources in the EGS and GOODS-N are identified as quasars with $L_X > 10^{44} \text{ erg s}^{-1}$. Because of the deep Chandra exposure in GOODS-S, most X-ray sources in this field have $L_X \sim 10^{42} \text{ erg s}^{-1}$. Only three have $L_X > 10^{43} \text{ erg s}^{-1}$, and none has $L_X > 10^{44} \text{ erg s}^{-1}$. These are consistent with expectations from the other fields, given the small area of GOODS-S (Table 1). Hickox et al. (2011) found that obscured AGNs selected from IRAC colors (Lacy et al. 2004; Stern et al. 2005) were equal in number to X-ray-selected AGNs. Regardless of the selection method, all of their AGNs had a clear visible–MIR color segregation from non-AGN galaxies.

Figure 3 shows the rest-frame 8 μm luminosity functions for galaxies in our sample, and Table 2 gives numerical values. The K -correction for L_8 was derived using the best-fit SED template for each galaxy as described in Section 3.1. We derived the luminosity function in the range $10 < \log_{10}(L_8/L_\odot) < 11.3$ using the $1/V_{\text{max}}$ method. There are a few existing 8 μm luminosity functions at various redshifts derived using the MIR photometry from either the Akari or Spitzer surveys (Caputi et al. 2007; Huang et al. 2007; Fu et al. 2010; Goto et al. 2015). We expect a strong evolution of the 8 μm luminosity function from $z = 1$ to $z = 0$ because of the cosmic SFRD evolution (e.g., Madau & Dickinson 2014) and the number evolution of LIRGs (e.g., Le Floch et al. 2005; Goto et al. 2015). Compared to the local 8 μm luminosity function, the luminosity function at $z \sim 1$ is either 10 times brighter or 10 times higher in number density or a mix of both. This is consistent with the cosmic SFRD decrease since $z \sim 1$.

Our sample’s total area coverage is only 694 arcmin², and most galaxies in the sample have $10 < \log_{10}(M_*/M_\odot) < 11$

¹⁷ The FIDEL legacy survey is described at <https://irsa.ipac.caltech.edu/data/SPITZER/FIDEL/>.

¹⁸ In this paper, L_{IR} means luminosity integrated between 8 and 1000 μm .

Table 1
The 16 μm Selected Sample

Field	Area arcmin ²	$f_{\text{limit}}(16\ \mu\text{m})$ μJy	# of Objects	# of z_{spec}	Redshift References ^a z_{spec} z_{phot}
EGS	432	130	263	190	Newman et al. (2013), Huang et al. (2013)
GOODS-N	158	30	334	264	Wirth et al. (2004), Dahlen et al. (2013)
GOODS-S	104	30	108	102	Balestra et al. (2010), Dahlen et al. (2013)
total	694		605	556	

Note.

^a Major surveys are indicated, but additional redshifts were collected from other publications.

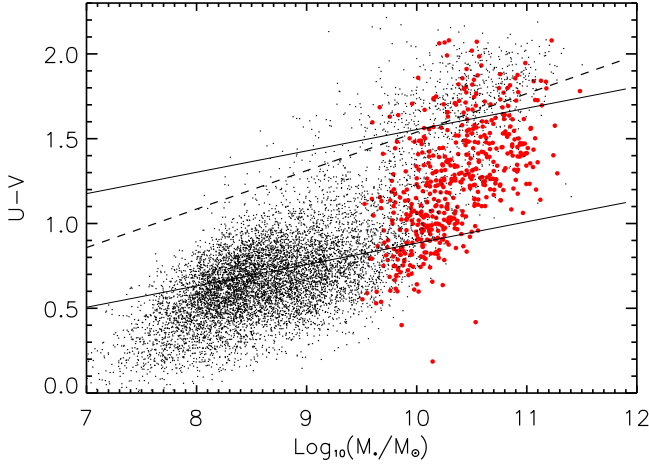


Figure 2. Color–mass distribution of galaxies. Red points indicate galaxies in our 16 μm selected sample. Black dots show comparison galaxies in the same redshift range from Fang et al. (2018). The horizontal coordinate represents the log of stellar mass in solar units, and the vertical coordinate represents the rest-frame $U - V$ color corrected for dust extinction. The typical uncertainties in the mass estimate are ~ 0.16 dex (Mobasher et al. 2015). The dashed line separates the “red sequence” from the “blue cloud” and “green valley” (Borch et al. 2006). The two solid lines show the upper and lower boundaries for the green valley for galaxies with $\log_{10}(M_*/M_\odot) > 10$ at $z \approx 1$ (Wang et al. 2017).

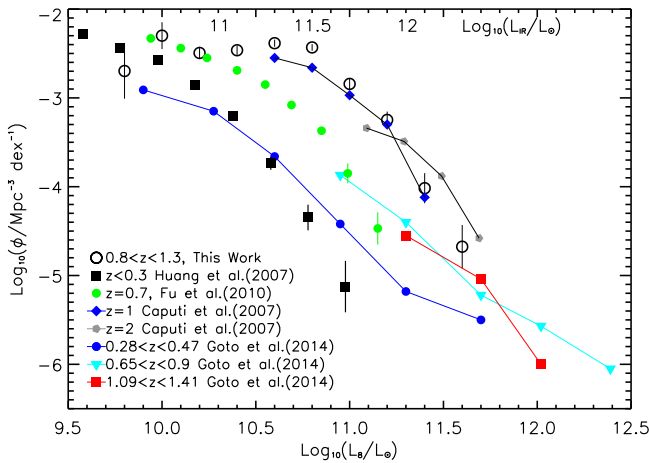


Figure 3. The rest-frame 8 μm luminosity function for 16 μm selected galaxies at $0.8 < z < 1.3$. This Work (open circles). Error bars are based on Poisson statistics, and the corresponding numerical data are in Table 2. Other symbols show rest-frame 8 μm luminosity functions from previous studies with redshifts indicated in the legend. Numbers near the upper abscissa indicate $\log_{10}(L_{\text{IR}}/L_\odot) = \log_{10}(L_8/L_\odot) + 0.7$. Some previous studies (Matute et al. 2006; Hopkins et al. 2007; Huang et al. 2007; Fu et al. 2010) are not plotted because their AGN subtraction is unclear.

Table 2
8 μm Luminosity Function at $z \approx 1$

$\log L_8/L_\odot$	$\log(\phi)^a$	$\delta \log(\phi)^a$
9.8	-2.95	0.43
10.0	-2.29	0.13
10.2	-2.47	0.07
10.4	-2.43	0.05
10.6	-2.33	0.04
10.8	-2.43	0.04
11.0	-2.76	0.05
11.2	-3.21	0.09
11.4	-4.01	0.17
11.6	-4.66	0.24

^a Units of ϕ are galaxies per comoving Mpc^{-3} for $H_0 = 70 \text{ km s}^{-1} \text{ Mpc}^{-1}$.

(Figure 2). This combination means the derived luminosity function will be subject to cosmic variance. This is especially the case for the GOODS-S field, which is roughly the size of the Ultra-Deep Field (UDF). According to Moster et al. (2011), cosmic variances are 34%, 25%, and 17% for galaxies in this mass range in UDF, GOODS-N, and EGS, respectively. The ICRAR cosmology calculator,¹⁹ based on the work of Driver & Robotham (2010) for local M^* galaxies, gives 25%, 23%, and 18% variance in areas equal to those of GOODS-S, GOODS-N, and EGS, respectively. In the three fields combined, the cosmic variance for this sample should be $\lesssim 20\%$.

3. MIR SEDs of Star-forming Galaxies and AGNs

3.1. Classifying the MIR Template Set

Most galaxy MIR spectroscopic studies have been for local galaxies. MIR spectral features from bright galaxies were first observed using ground-based telescopes. (Moorwood 1986 and Roche et al. 1991 gave useful summaries of early work.) Spectra of star-forming galaxies show strong PAH emission features at 3.3, 6.2, 7.7, 8.6, and 11.3 μm . In contrast, AGNs show strong continuum emission in this wavelength range and often show broad silicate absorption from 8 to 13 μm . With its launch in 1995, the ISO made MIR spectroscopy possible for samples of IR-luminous galaxies (Genzel et al. 1998; Rigopoulou et al. 1999). Starting in 2003, Spitzer/IRS spectroscopy provided even better sensitivity than ISO, allowing spectroscopic observations of extragalactic sources with luminosities ranging from local dwarf galaxies to ULIRGs/HyperLIRGs (ultra- and hyperluminous infrared galaxies) at $z \sim 2$ (Brandl et al. 2006; Spoon et al. 2007).

¹⁹ <https://cosmolcalc.icrar.org/>

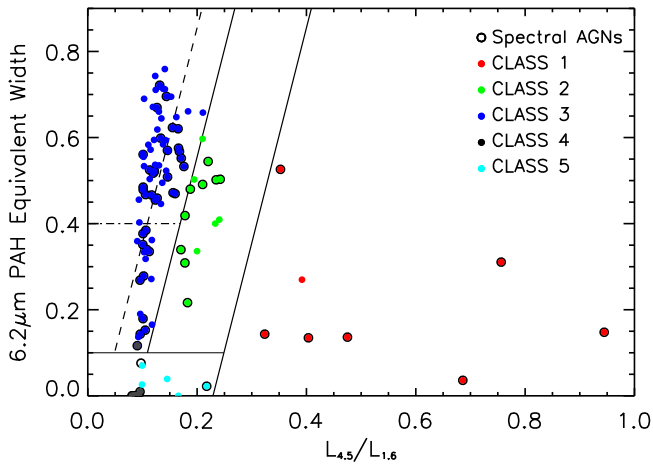


Figure 4. MIR classification diagram for 129 local SED templates from Brown et al. (2014). Points show each template’s $6.2 \mu\text{m}$ PAH feature EW vs. its $L_{4.5}/L_{1.6}$ ratio. The dashed line shows the relation of Equation (1), which was derived from Class 3 points with $\text{EW} > 0.4$ (dashed-dotted line). Points with black borders indicate templates derived from AGNs. Lines show boundaries of the five template classes. Class 1 templates are those with a high MIR continuum and consequently low PAH EW, characteristic of strong AGNs. Class 2 templates have higher EW, characteristic of composite AGN + star-forming galaxies. Class 3 templates are for star-forming galaxies with PAH emission features. Class 4 are for quiescent galaxies with no dust emission. They are not labeled in the figure but cluster around (0.09, 0). Class 5 templates are for uncommon blue-compact or Wolf–Rayet galaxies (Wu et al. 2008) with relatively blue $L_{4.5}/L_{1.6}$ colors. Table 3 gives the numerical values for the template boundaries.

Even now, however, spectra of distant galaxies are limited in number.

There are a few sets of broadband galaxy SED template sets with wavelength coverage extending from the ultraviolet (UV) to $30 \mu\text{m}$ (e.g., Polletta et al. 2007; Assef et al. 2008, 2010; Brown et al. 2014). We chose the set from Brown et al. (2014), consisting of an atlas of 129 local-galaxy SED templates based on spectral and photometric data observed with ground-based telescopes, Spitzer/IRS, and Akari/IRC. Templates include a wide range of SED and morphological types representative of the local population, and they have $9 < \log(L_{\text{IR}}/L_{\odot}) < 12$ based on IRAS and Herschel FIR photometry (Dale et al. 2012, 2017).

For this work, we divided the Brown et al. (2014) templates into five distinct classes²⁰ characterized by their predominant energy sources: star formation, starlight, and AGNs. In order to avoid the effects of dust obscuration, classes were based only on rest-frame $1 \mu\text{m} < \lambda < 30 \mu\text{m}$. In this wavelength range, PAH emission bands are the predominant spectral features. The $6.2 \mu\text{m}$ PAH equivalent width (EW) is a good indicator of AGN strength (Alonso-Herrero et al. 2012) with a mean $6.2 \mu\text{m}$ $\text{EW} = 0.24 \pm 0.19$ for strong AGNs, 0.44 ± 0.06 for composite galaxies, and 0.52 ± 0.06 for galaxies with H II spectral types. An additional classification parameter is needed because the Brown et al. (2014) template set contains galaxies with a much wider luminosity range and more diverse spectral types than does the Alonso-Herrero et al. (2012) LIRG sample. We used the $L_{4.5}/L_{1.6}$ color, as shown in Figure 4, to characterize the SED shapes. A galaxy’s $4.5 \mu\text{m}$ emission may come from three components: stellar photospheres, star formation regions, and AGN. Huang et al. (2007) found that when star formation

activity contributes to the MIR continuum, it is correlated with PAH emission. Figure 4 shows typical elliptical galaxies have $L_{4.5}/L_{1.6} \approx 0.085$. Galaxies with $6.2 \mu\text{m}$ PAH $\text{EW} > 0.4$ tend to have higher $L_{4.5}/L_{1.6}$ as star formation begins to contribute. Galaxies with high $L_{4.5}/L_{1.6}$ and low $6.2 \mu\text{m}$ PAH EW harbor AGNs. A linear relation (fit with iterative σ -clipping to points above $\text{EW} = 0.4$) gives

$$\text{EW} = 5 \times (L_{4.5}/L_{1.6} - 0.029). \quad (1)$$

Figure 4 shows how the template classes are defined. Star-forming galaxy templates have $\text{EW} > 0.1 \mu\text{m}$ and $L_{4.5}/L_{1.6}$ within 3σ of the corresponding value from Equation (1). AGN templates have $L_{4.5}/L_{1.6}$ more than 10σ greater than the Equation (1) value. Templates with offsets between 3σ and 10σ and $\text{EW} > 0.1$ are defined as composite. About one-third of all templates are from spectroscopically identified AGN hosts, but some of these show almost no MIR spectral signature of an AGN. This happens when the AGN luminosity is relatively small compared to the star formation luminosity. Templates with no PAH emission features come from galaxies visually classified as either elliptical or blue compact or Wolf–Rayet type. Table 3 specifies the color–EW boundaries of our five classes.

The templates in each class resemble each other and differ from templates in other classes as shown in Figures 5–9. Class 1 templates represent AGNs, and Class 2 templates represent composite galaxies. Star-forming templates (Class 3) have strong PAH emission features. Quiescent templates (Class 4) have nearly Rayleigh–Jeans SEDs typical of starlight. Class 5 templates show a dust continuum starting to rise at $5\text{--}6 \mu\text{m}$ with little PAH emission. These nine templates (Figure 9) have a strong [S IV] emission line at $10.5 \mu\text{m}$. The local galaxies in Class 5 are either young, blue, and compact or Wolf–Rayet galaxies (Wu et al. 2008), consistent with the strong [S IV] line (Inami et al. 2013).

When spectral information is not available, a color–color diagram can be used to classify galaxies though with some uncertainty as shown in Figure 10. Galaxies with significant star formation (Class 3) have a strong correlation between $L_{4.5}/L_{1.6}$ and $L_8/L_{1.6}$:

$$L_8/L_{1.6} = 11.8(L_{4.5}/L_{1.6} - 0.0788), \quad (2)$$

as shown in Figure 11, indicating that dust emission associated with star formation produces the MIR continuum (Huang et al. 2007). Strong AGN (Class 1) templates have SEDs resembling a power law with $4.5 \mu\text{m}$ emission not much less than that at $8 \mu\text{m}$. Composite (Class 2) templates resemble Class 3 but have slightly more $4.5 \mu\text{m}$ emission than the corresponding star-forming templates as a result of the AGN contribution.

3.2. SED Fitting with the Local-galaxy Template Set

We fit SEDs only in the observed MIR wavelength range $3.6 \mu\text{m} < \lambda < 24 \mu\text{m}$. At $z = 1$, this corresponds to rest-frame $1.8 \mu\text{m} < \lambda < 12 \mu\text{m}$, where a galaxy SED has PAH emission and silicate absorption features and is little affected by dust extinction. In order to calculate the χ^2 of the fits, we recalculated photometric uncertainties by putting artificial objects into the published images and measuring the photometric errors. EGS has shallower IRAC and $16 \mu\text{m}$ depth than the GOODS fields and yields larger uncertainties. Our SED

²⁰ We use “Class” instead of “Type” to avoid confusion with the well-defined Type 1 and 2 AGNs.

Table 3
Template Classification Criteria

Template	Type	6.2 μm PAH EW	$L_8/L_{1.6}$
Class 1	AGN		$(5 \times L_{4.5}/L_{1.6}) - \text{EW} > 1.145$
Class 2	Composite	$\text{EW} > 0.1$	$1.145 > (5 \times L_{4.5}/L_{1.6}) - \text{EW} > 0.445$
Class 3	Star-forming	$\text{EW} > 0.1$	$(5 \times L_{4.5}/L_{1.6}) - \text{EW} < 0.445$
Class 4	Quiescent	$\text{EW} = 0$	$L_{4.5}/L_{1.6} \sim 0.1$
Class 5	Blue Compact	$\text{EW} < 0.1$	$L_{4.5}/L_{1.6} < 0.25$

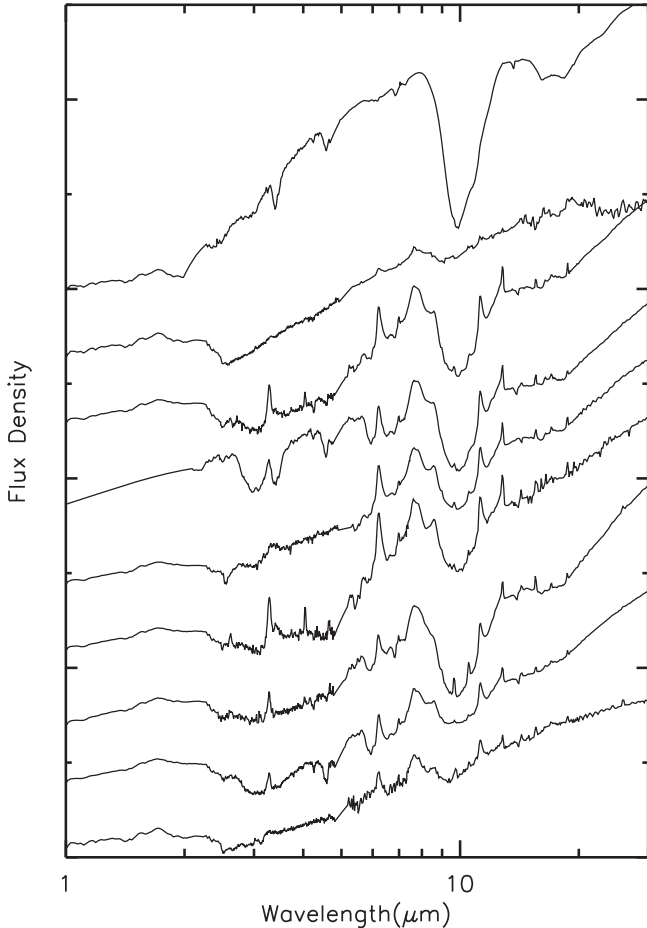


Figure 5. The nine Class 1 SED templates from Brown et al. (2014). All have strong continuum emission from the central AGN, and many show the 9.7 μm silicate feature in absorption.

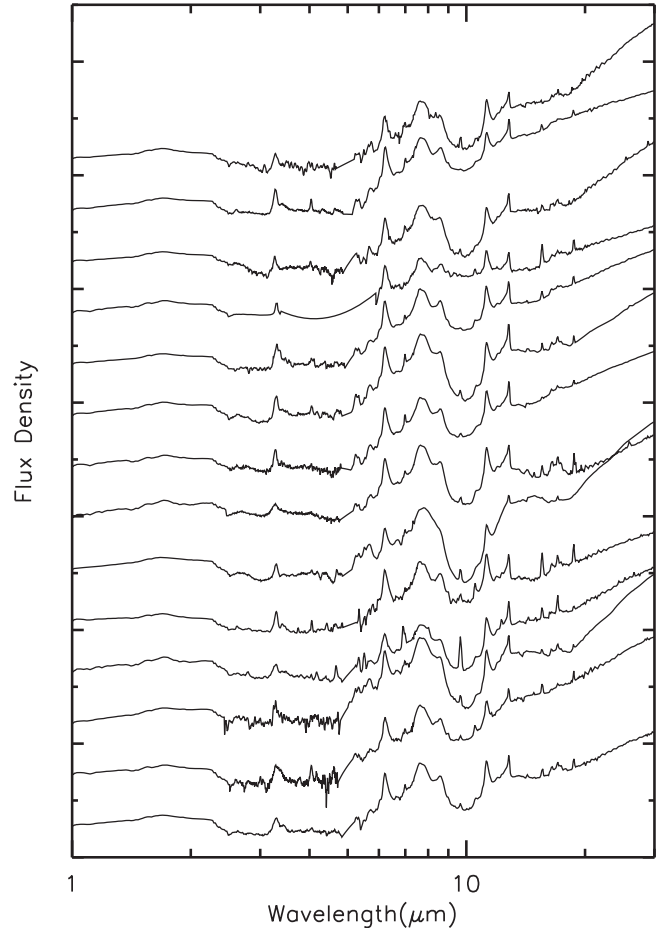


Figure 6. Examples of Class 2 SED templates from Brown et al. (2014). A representative 18 are shown out of 20 in the complete set. The templates have composite SEDs with both star-forming and AGN features in the MIR.

fitting gave a reduced $\chi_r^2 < 2$ for 447 galaxies in the sample, and only 21 have $\chi_r^2 > 10$ (Figure 12). Table 4 gives the best-fit template class distribution for each field. No sources in the entire sample were fit by Class 4 (quiescent galaxy) templates. Detecting a pure-starlight passive galaxy at 16 μm , even in the deep GOODS fields, would require $M_* > 3 \times 10^{11} M_\odot$. Such massive galaxies are rare, and failing to detect even one in the area surveyed is no surprise.

The best fits are for star-forming galaxies, as shown by the lower χ_r^2 values in Figure 12. The Class 3 template set covers a wide range of colors and PAH EWs as shown in Figures 4 and 10, and therefore, it is not surprising that a good template can nearly always be found. Figures 13 and 14 show examples of good fits with star-forming templates.

Fitting SEDs for galaxies with Class 1 (AGN) templates yields a slightly higher reduced χ_r^2 than for star-forming

galaxies. Examples are shown in Figure 15. While AGN variability could be a factor at the 0.1 mag level (Kozłowski et al. 2016), two related factors likely contribute more to the higher χ_r^2 . One is that our $z \approx 1$ AGNs are much more luminous than local ones and may not be represented in the local templates. The other is that there are only nine Class 1 templates in the set, and these may not represent the full range of AGN SEDs even among local galaxies. A further contributing factor is that the AGN galaxies generally have high signal-to-noise ratios (S/Ns), and therefore, even minor deviations from the templates will give large χ_r^2 . Figure 10 shows the wide range of color space the AGNs map out and the paucity of templates within that space. Figure 5 shows that the templates include not only a range of continuum slopes but also multiple absorption and emission features, e.g., water absorption at 3.1 μm , PAH emission at 3.3 μm , and the bare carbon

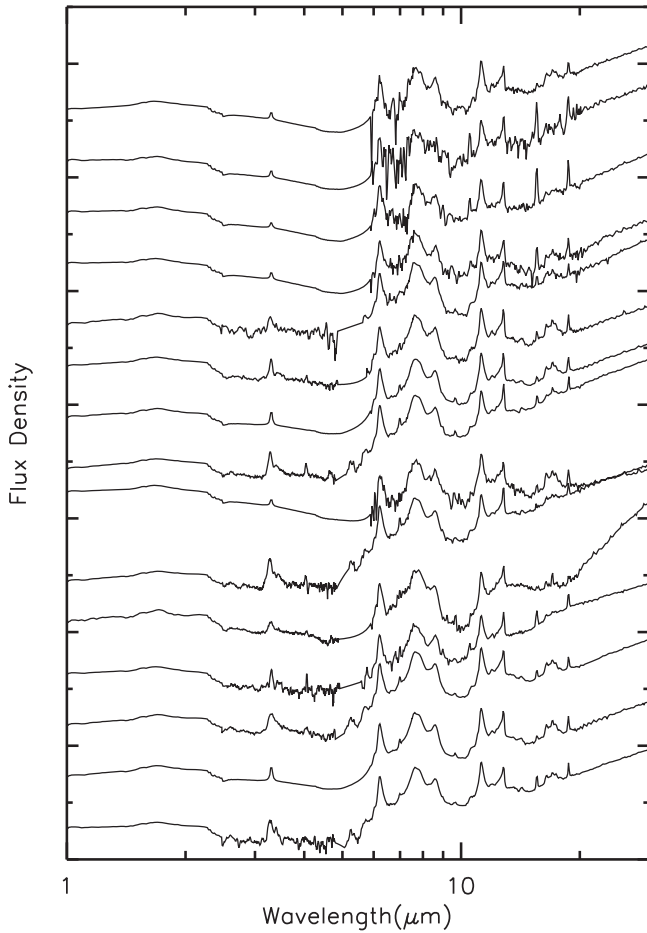


Figure 7. Examples of Class 3 SED templates from Brown et al. (2014). A representative 17 are shown out of 68 in the complete set. The templates are those of star-forming galaxies with strong PAH emission features.

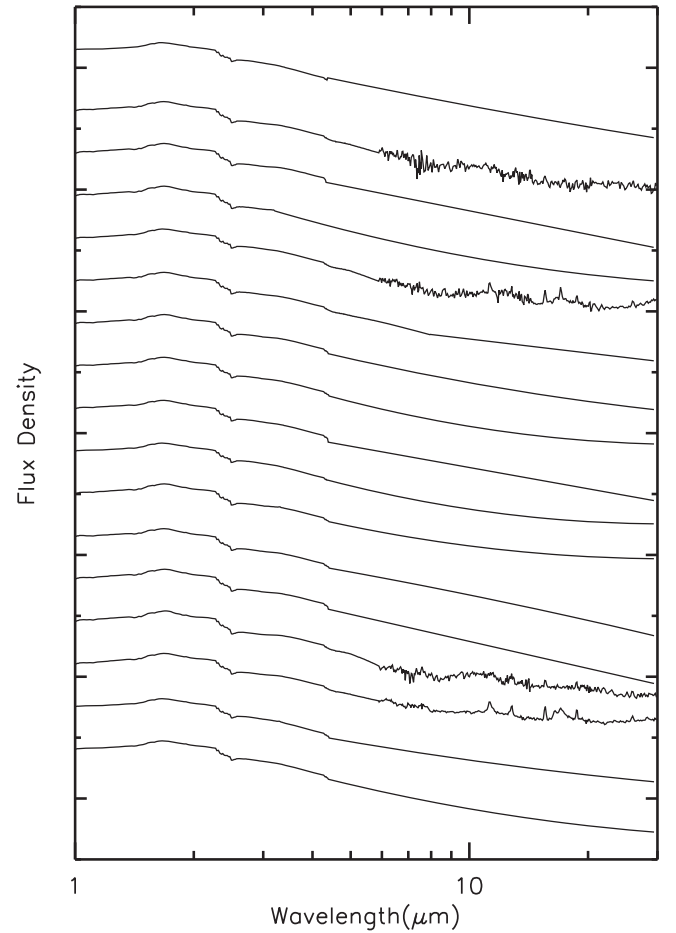


Figure 8. Examples of Class 4 SED templates from Brown et al. (2014). A representative 17 are shown out of 23 in the complete set. The templates are those of quiescent galaxies with little or no dust emission.

absorption feature at $3.4 \mu\text{m}$ (Imanishi et al. 2001). Nine templates are simply not enough to cover the full range of parameters. An example is shown in Figure 16, where the local UGC 5101 template includes lots of features but still deviates from the observed GOODS N-54 SED.

With only six photometry points for each object used in template fitting, multiple templates might fit an observed SED within the uncertainties. To evaluate such degeneracies, we compared the best and the second-best templates for each galaxy. We defined a χ_r^2 limit as $\exp(-\chi_1^2)/\exp(-\chi_2^2) < 1.5$, where χ_i are the reduced χ for the best and second-best templates, respectively. There are 262 galaxies within this limit. In 170 of them, both templates belong to the same class. For 86 objects, the two templates belong to adjacent classes, either Class 1 and Class 2 or Class 2 and Class 3. Only six objects have one of the two best-fit templates from Class 1 and the other from Class 3. All of these six are in the EGS field, where larger photometric errors may contribute. In summary, most cases of degenerate template-fitting results are due to the similarities between the templates as shown in Figures 4 and 10, and the majority of our sample have a clear SED identification.

The fitting procedure identified nine objects in the sample with weak or absent $8 \mu\text{m}$ PAH in their SEDs but red continua near that wavelength. The best fits to these objects are SEDs of UGCA 166, UGCA 219, UGCA 410, and Mrk 930. These

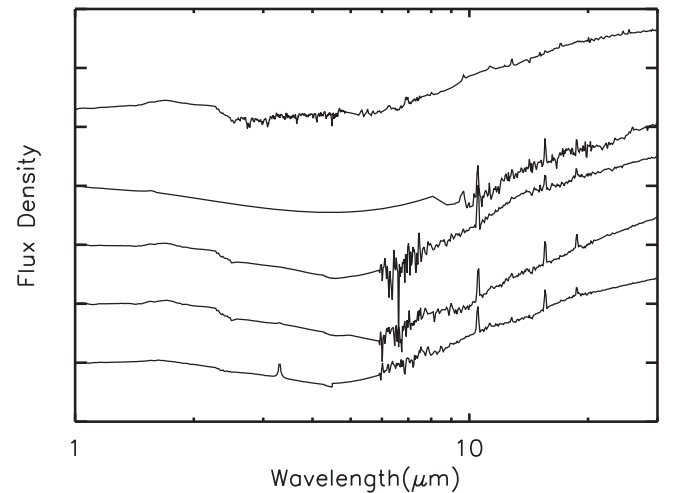


Figure 9. Five Class 5 SED templates from Brown et al. (2014). The templates are those of blue compact or Wolf-Rayet galaxies with little or no PAH emission but with dust emission starting to rise steeply at $\sim 6 \mu\text{m}$ (Wu et al. 2008). These templates have much lower $L_{4.5}/L_{1.6}$ than the Class 1 templates.

Class 5 templates show no or extremely weak PAH features (Wu et al. 2008), but unlike normal AGNs whose strong continuum emission starts around $3 \mu\text{m}$, their hot dust emission starts around rest-frame $6 \mu\text{m}$ (Figure 17). Local galaxies with

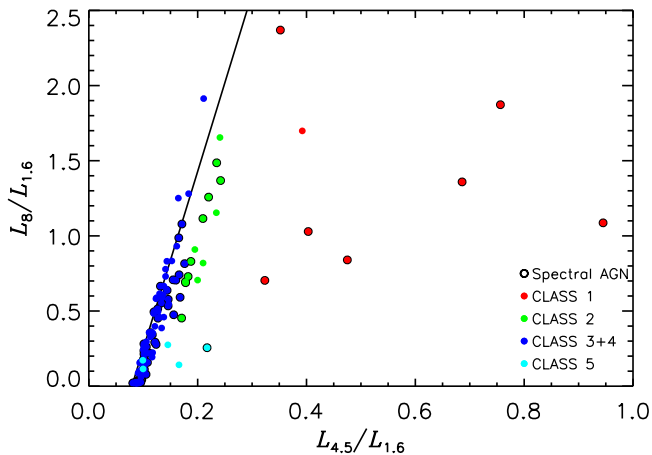


Figure 10. MIR–NIR color–color diagram for the template set. The ratio $L_8/L_{1.6}$ roughly traces the specific star formation rate, while $L_{4.5}/L_{1.6}$ basically traces the AGN luminosity per stellar mass. Template types are shown by colors as indicated in the legend. The line shows the best-fit relation for star-forming templates (Equation (2)).

this MIR SED are typically Wolf–Rayet or blue compact galaxies with $M_* < 10^9 M_\odot$. The lack of PAH emission is a result of either low metallicity (Engelbracht et al. 2005; G. Jin et al. 2021, in preparation) or vigorous star formation with intense UV radiation destroying PAH molecules. The existence of OB stars and intense UV radiation in local galaxies of this type is supported by the detection of the [S IV] $\lambda 10.54 \mu\text{m}$ and He II $\lambda 4686 \text{ \AA}$ lines in their spectra. Ionization potentials are $\sim 35 \text{ eV}$ and $\sim 25 \text{ eV}$, respectively, demanding the presence of hard UV photons to produce the lines. Recent Herschel and ALMA observations of blue compact galaxies UGCA 166 and SBS 0335–052 found FIR SED peaks between 20 and $60 \mu\text{m}$ (Hunt et al. 2014), indicating high dust temperatures in these systems. This is consistent with a strong UV radiation from compact star formation regions. Previous studies concluded that these two galaxies are very young with $M_* \sim 10^6 M_\odot$ (Houck et al. 2004; Wu et al. 2008; Hunt et al. 2014). However, the nine objects in our sample fitting Class 5 templates have $M_* > 10^{10.5} M_\odot$. They are therefore unlikely to have low metallicity or be in the early stages of star formation. The galaxies show no strong X-ray emission or excess continuum emission at rest-frame $4.5 \mu\text{m}$, making AGN an unlikely cause for the absence of PAH. Further study of this population is needed.

3.3. AGNs in the $16 \mu\text{m}$ Selected Sample

Our SED results identify that about 15% of galaxies in the sample are best fit by local AGN templates, and another 32% have composite SEDs with both AGN and star formation contributions. Confirmation of AGNs through spectroscopy is challenging, and we therefore resorted to X-ray observations (Nandra et al. 2015; Xue et al. 2016; Luo et al. 2017) for AGN confirmations. About 18% of the whole $16 \mu\text{m}$ sample are X-ray detected. Table 5 gives the X-ray depth of each field and the percentages of X-ray detections for each field in each class. In all fields, Class 1 sources were detected at a much higher rate than other classes, consistent with the AGN classification. However, even with the 7 Ms depth in GOODS-S, fewer than half of the presumed AGNs were X-ray detected.

Nandra et al. (2015), Xue et al. (2016), and Luo et al. (2017) derived physical properties from the X-ray SEDs including

Table 4
SED Classes for the $16 \mu\text{m}$ Selected Sample

Field	Class 1 AGN	Class 2 Composite	Class 3 Star-forming	Class 5 Blue Compact
EGS	43	78	142	0
GOODS N	49	115	161	9
GOODS S	15	30	63	0
All	107	223	366	9
Fractions	15.2%	31.6%	51.9%	1.3%

X-ray luminosities and obscuration expressed as gas column density N_{H} . Figure 18 shows that about 70% of the X-ray AGNs in this sample have $N_{\text{H}} > 10^{22} \text{ cm}^{-2}$, which corresponds to visual extinction $A_V \approx 5 \text{ mag}$ (Valencic & Smith 2015), i.e., a dusty AGN. Three X-ray sources have $N_{\text{H}} \gtrsim 10^{25} \text{ cm}^{-2}$, qualifying them as Compton-thick. They have apparent $L_X \gtrsim 10^{44} \text{ erg s}^{-1}$, in the classical AGN range, but none of these three objects has a Class 1 SED, and two are Class 3. With such large extinction, the true X-ray luminosity is uncertain and may be lower than estimated. A more important factor may be the extinction, which corresponds to $A_V \approx 500 \text{ mag}$ and $A_{4.5 \mu\text{m}} \approx 23 \text{ mag}$ (Hensley & Draine 2020). Figure 18 shows other, less extreme examples of X-ray-luminous objects with Class 3 SEDs. While the extinction amounts are uncertain, AGNs can be so well hidden that MIR SEDs reveal no trace of them. Figure 19 shows the distribution of SED Classes for four ranges of X-ray luminosity. Almost all X-ray sources with $L_X > 10^{44} \text{ erg s}^{-1}$, i.e., the X-ray QSOs, have Class 1 SEDs. In contrast, most X-ray sources with $L_X < 10^{42} \text{ erg s}^{-1}$ have a Class 3 SED, indicating that they are predominantly star-forming galaxies. X-ray sources with intermediate luminosity show a range of classes including many composites. Overall, the percentage of objects with Class 1 SEDs increases with X-ray luminosity, showing a good correlation between the X-ray luminosity and MIR SED Class.

Our SED fitting also yields an accurate measurement of MIR luminosities characterizing both star formation and AGN. Several studies showed a correlation between AGNs’ MIR and X-ray luminosities (e.g., Carleton et al. 1987; Lutz et al. 2004; Fiore et al. 2009; Lanzuisi et al. 2009; Stern 2015; Suh et al. 2019). This correlation was found for AGNs with $L_X > 10^{42} \text{ erg s}^{-1}$, which have strong MIR continuum emission (Stern 2015; Dai et al. 2018) and is the same for Type 1 (broad-line) and Type 2 (narrow line) AGNs (Suh et al. 2019). Luminosity at rest-frame $6 \mu\text{m}$, L_6 , was often used to represent the MIR luminosity in these previous studies. Most of the X-ray sources in our sample also have PAH emission in the MIR bands. This is consistent with many Class 1 templates (Figure 5) and all the Class 2s and 3s (Figures 6 and 7) and is probably a result of the $16 \mu\text{m}$ sample selection favoring sources having $7.7 \mu\text{m}$ emission features. PAH emission being present means that L_6 could be contaminated by the $6.2 \mu\text{m}$ feature. We therefore used rest-frame $4.5 \mu\text{m}$ luminosity as an MIR measure of AGN accretion power. L_8 and $L_{4.5}$ were directly derived from each object’s SED. These luminosities come from both star formation and AGN. As explained in the Appendix, the excess luminosity at $4.5 \mu\text{m}$, attributed to an AGN, is

$$L_{4.5}^{\text{Exc}} = L_{4.5} - L_{4.5}^{\text{SFR}} = \epsilon(11.8L_{4.5} - L_8 + 0.93L_{1.6}), \quad (3)$$

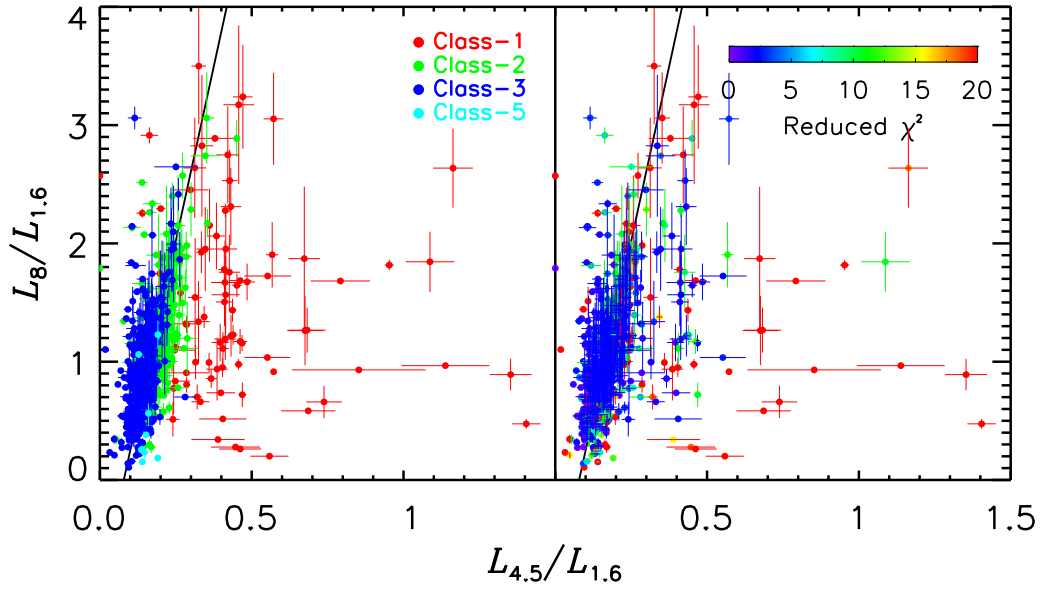


Figure 11. Color–color diagram for the 16 μm selected sample galaxies. Points in the left panel are color-coded by SED type as indicated in the legend. Colors in the right panel indicate the reduced χ^2 as indicated in the color bar. The line shows the color–color relation for the Class 3 and 4 templates from Figure 10.

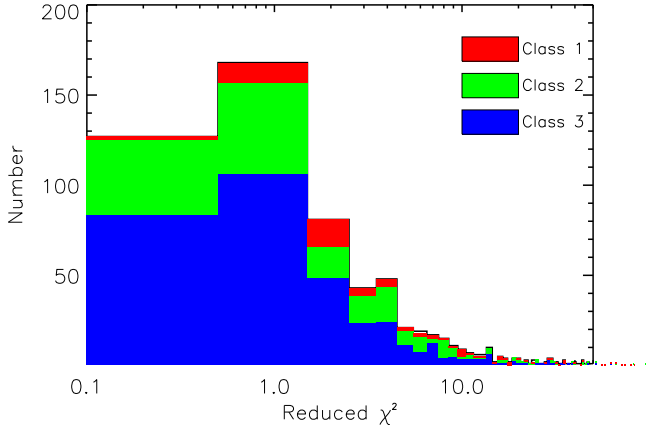


Figure 12. Histogram of reduced χ^2 of all SED fits for the 705 galaxies in the sample. The color bars are counts for galaxies with different SED classes. Class 5 templates are not shown but have $0.5 < \chi_r^2 < 50$.

where $\epsilon \approx 0.093$. Objects with $L_{4.5}^{\text{Exc}}/\sigma_{4.5}^{\text{Exc}} > 3$ are those with a significant excess. (Flux density uncertainties at both 8 and 16 μm contribute to $\sigma_{4.5}^{\text{Exc}}$, the uncertainty of $L_{4.5}^{\text{Exc}}$.) It is not surprising that most $L_{4.5}$ -excess objects have an SED best fit by Class 1 templates, as shown in Figure 20. There is a good correlation between $L_{4.5}^{\text{Exc}}$ and L_X for X-ray sources in our sample, as shown in Figure 21. The best fit is

$$\log_{10}(L_{4.5}^{\text{Exc}}/L_{\odot}) = 0.85 \log_{10}(L_X/10^{42} \text{ erg s}^{-1}) + 9.19. \quad (4)$$

X-ray sources at $L_X < 10^{42} \text{ erg s}^{-1}$ could be powered purely by star formation, but a few of these have high $L_{4.5}^{\text{Exc}}$ and Class 1 SEDs, indicating their AGN nature. These may be X-ray-obscured. The correlation between L_X and $L_{4.5}^{\text{Exc}}$ suggests that the excess MIR luminosity is a signature of the active nucleus and can be used as a measure of AGN luminosity.

There are many galaxies in the sample with strong $L_{4.5}^{\text{Exc}}$ but no X-ray detection. The 3σ and 5σ limits are roughly at $\log_{10}(L_{4.5}^{\text{Exc}}/L_{\odot}) = 9.5$ and 10. According to Equation (4), the two limits roughly correspond to $L_X = 10^{42.1}$ and $10^{43} \text{ erg s}^{-1}$,

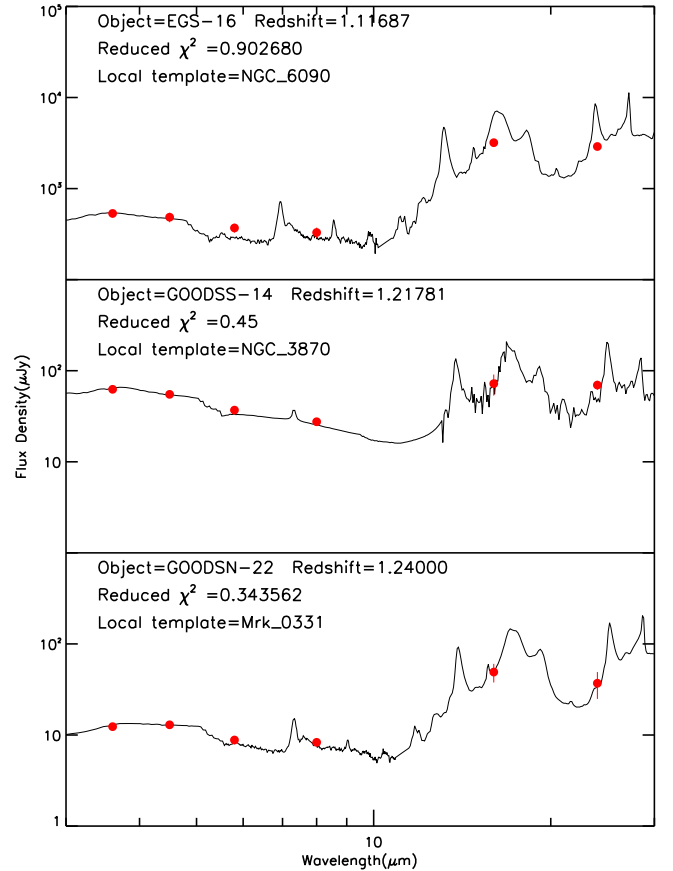


Figure 13. Examples of galaxy SEDs best fit with a Class 3 (star-forming) template. Lines show the best-fit template, which is identified in each panel. Points show the observed photometric data. Wavelengths are in the observed frame, and redshifts are given in the panel text.

respectively. AGNs at these X-ray luminosities should have been detected by Chandra, but only half of them were. This is consistent with at least half of all AGNs being obscured in X-rays (Gilli et al. 2007; Hickox & Alexander 2018; Lambrides et al. 2020). We did not find any significant difference between

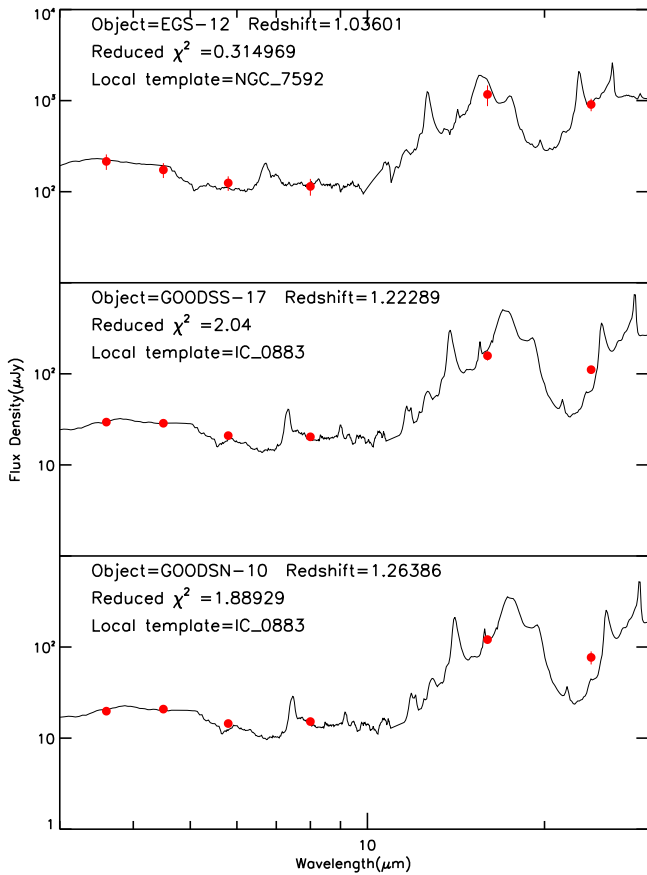


Figure 14. Examples of galaxy SEDs best fit with a Class 2 (composite) template. Lines show the best-fit template, which is identified in each panel. Points show the observed photometric data. Wavelengths are in the observed frame, and redshifts are given in the panel text.

the MIR-excess-selected objects with and without X-ray detection, but as shown in Figure 22, the percentage of X-ray-detected sources increases with exposure time and with luminosity $L_{4.5}^{\text{Exc}}$. This trend suggests that the MIR-excess targets without X-ray detections are X-ray-obscured, at least in the GOODS fields. (In the EGS, the relatively shallow X-ray depth may also play a role.) Selecting on the basis of MIR excess $L_{4.5}^{\text{Exc}}/\sigma_{4.5}^{\text{Exc}} > 3$ gives 140 objects. Of these, 63 have a Class 1 SED, 45 have a Class 2 SED, and 32 have a Class 3 SED. In the first category, all the Class 1 templates have a MIR excess, but with the available S/N, the simple $L_{4.5}^{\text{Exc}}$ calculation finds only about 60% of the individual objects fitting the AGN templates. The 32 Class 3 objects with detectable MIR excess are 9% of all Class 3 objects. Even though their MIR emission is powered mainly by star formation, these objects show a detectable amount of AGN emission. There might be another 4% or so that would show an excess if higher S/N observations were available. The overall number of AGNs found by MIR excess is about double the number of $L_X > 10^{42}$ erg s $^{-1}$ AGNs in this sample (Table 5). The combination of MIR and X-ray selection yields a more complete AGN sample than X-ray selection alone, as has been found before (Hickox et al. 2011).

4. Star Formation in the 16 μm Selected Galaxies

4.1. SFR Estimators from the UV to FIR

One goal of this project is to compare various SFR estimators for galaxies. Our sample has luminosities available

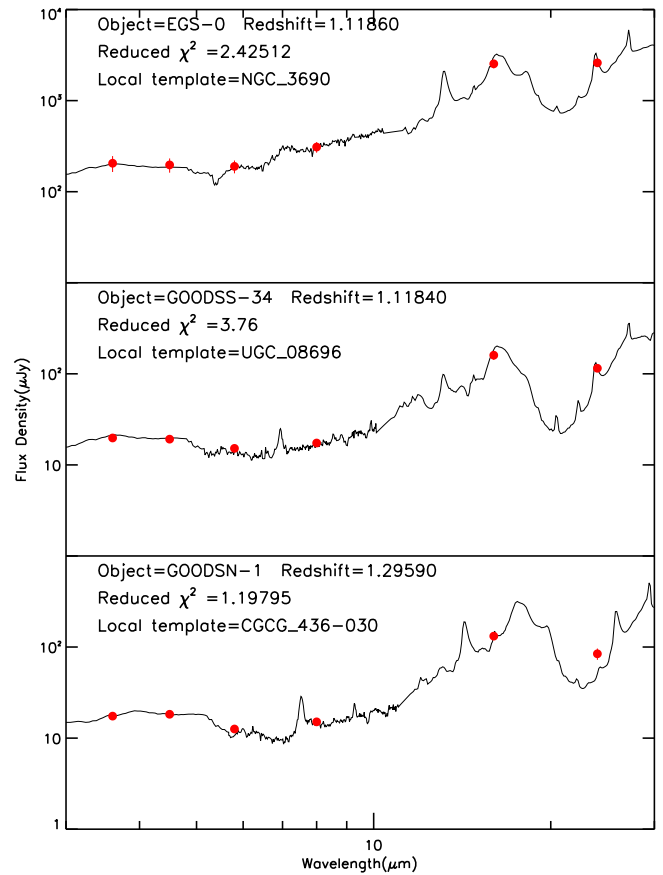


Figure 15. Examples of galaxy SEDs best fit with a Class 1 (AGN) template. Lines show the best-fit template, which is identified in each panel. Points show the observed photometric data. Wavelengths are in the observed frame, and redshifts are given in the panel text.

in the UV, MIR, and FIR, all of which can be used to estimate the SFR. For this work, SFR_{UV} was calculated from UV-visible SED modeling of CANDELS data (Grogin et al. 2011), including dust correction (Fang et al. 2018). $\text{SFR}_{8\mu\text{m}}$ was based on L_8 (rest frame as derived from the 16 μm photometry) converted to SFR according to the Elbaz et al. (2011) conversion. SFR_{24} was calculated using the observed 24 μm flux density and an appropriate template (Chary & Elbaz 2001). SFR_{FIR} was based on the L_{IR} from Herschel FIR SEDs. We excluded galaxies with significant $L_{4.5}^{\text{Exc}}$ to avoid confusion by AGN contamination. Fang et al. (2018) found SFR_{UV} and SFR_{24} to be consistent for $z < 1.5$ galaxies. Figure 23 shows that all SFR estimates yield consistent results on average, but $\text{SFR}_{\text{UV,corr}}$ shows considerably more scatter with the other three indicators than any of them shows with another. There is a slight trend for SFR_{24} to be lower than the other SFRs at the lowest masses. Some galaxies have very low SFR_{UV} , probably because the modeling underestimated dust extinction. Though there are arguments that PAH emission may vary when tracing SFRs due to metallicity difference (G. Jin et al. 2021, in preparation) or heating from evolved stars (Crocker et al. 2013), the correlation between SFR and PAH luminosity has held up, albeit with scatter (Treyer et al. 2010), or some systematics at low and high luminosity (Mahajan et al. 2019). Elbaz et al. (2011) found $\text{SFR}_{8\mu\text{m}}$ to be better than SFR_{24} at $z > 2$. Our results show that L_8 is a good SFR estimator for this LIRG sample at $z \sim 1$, indicating that the PAH emission is associated with star-forming regions in these LIRGs.

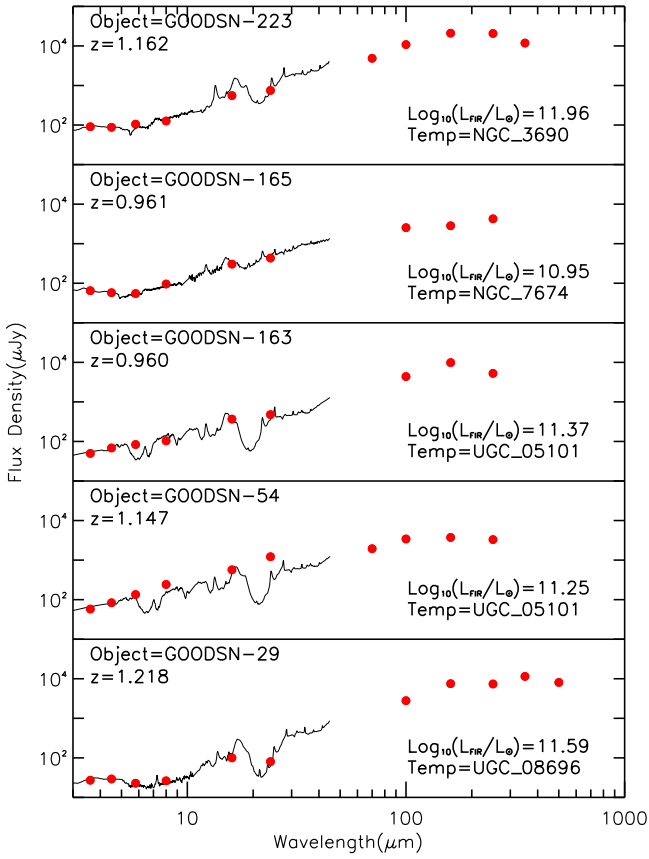


Figure 16. Full IR SEDs for galaxies with dominant AGN contribution in the MIR (Class 1). Only galaxies with positive detections in at least three Herschel bands are shown. Lines show the templates, and points show the observed data. Photometric uncertainties are smaller than the point sizes. Wavelengths are in the observed frame, and redshifts are given in the panel text.

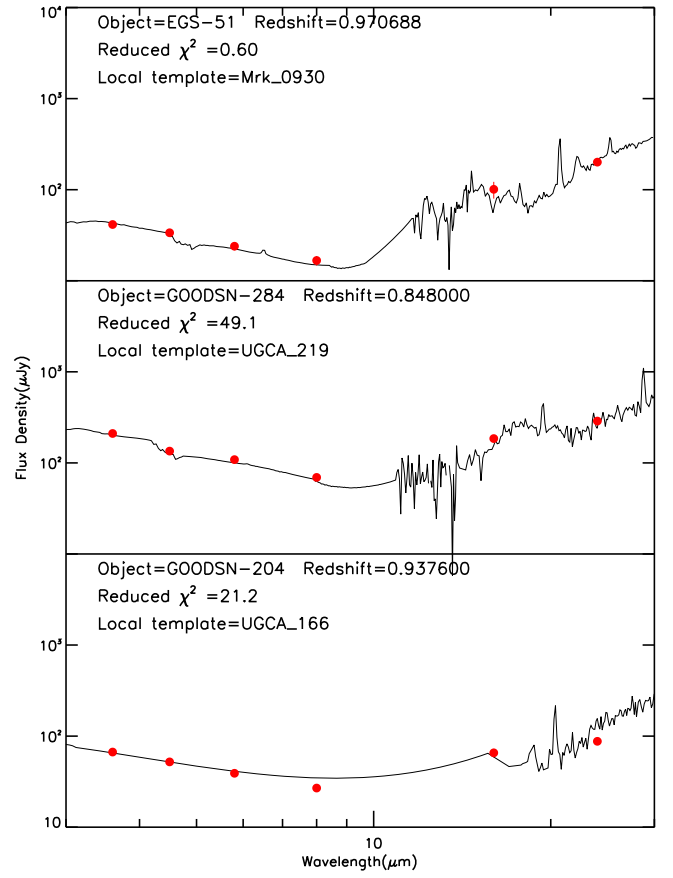


Figure 17. Examples of galaxy SED best fit with Class 5 (Wolf-Rayet or blue compact) templates. Lines show the best-fit template, which is identified in each panel. Points show the observed photometric data. Wavelengths are in the observed frame, and redshifts are given in the panel text. Our sample has only 10 objects of this type.

Table 5
Number of Each SED Class Detected in X-Rays

Field	Chandra exp. Time	Class 1 AGN	Class 2 Composite	Class 3 Star-forming
All Chandra X-ray detections				
EGS	0.8 Ms	7	10	7
GOODS-N	2 Ms	22	17	16
GOODS-S	7 Ms	12	10	24
With $L_x > 10^{42}$ erg s $^{-1}$				
EGS		7	10	7
GOODS-N		20	9	10
GOODS-S		4	2	2

Note. Xue et al. (2016) and Luo et al. (2017) reported X-ray luminosities for GOODS-N and GOODS-S, respectively, for the energy band 0.7–7 keV. To be consistent with EGS luminosities, we have converted to luminosities in the 2–10 keV band by multiplying by 0.721.

4.2. Star Formation in AGNs

As shown above, AGNs tend to produce MIR emission, which will cause overestimated SFR if not excluded. The Appendix shows how to solve a set of linear equations to separate the components into L_8^{SFR} and $L_{4.5}^{\text{Exc}}$. For most galaxies, the AGN correction from L_8 to L_8^{SFR} and the star formation correction from $L_{4.5}$ to $L_{4.5}^{\text{Exc}}$ are modest. Figure 24

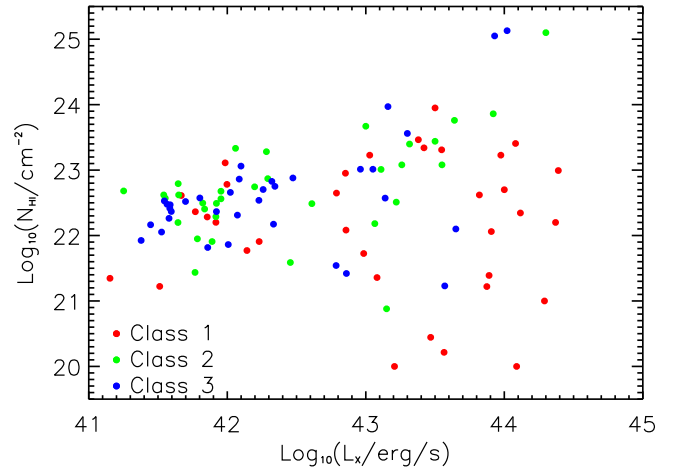


Figure 18. H I column densities for all X-ray sources in the sample. Colors indicate SED class as indicated in the legend. The three X-ray sources with $L_x \sim 10^{44}$ erg s $^{-1}$ and not Class 1 are at the top of the plot.

shows that for most objects, an AGN contributes at most 10%–20% of L_8 . However, for $L_{4.5}^{\text{Exc}} > 10^{9.5} L_{\odot}$, L_8 will overestimate SFR for a significant fraction of galaxies, nearly all of them having Class 1 SEDs. In the whole sample, 20 galaxies have $L_8^{\text{SFR}}/L_8 < 0.5$, and a few have L_8^{SFR} consistent with zero. For these objects, neither L_8 nor L_{24} is a good SFR estimator. The

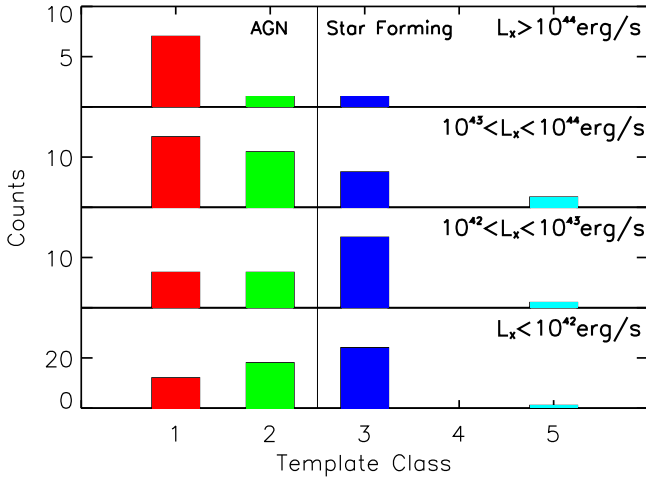


Figure 19. Histograms showing SED classes for Chandra X-ray sources in our 16 μm selected sample. Rows show galaxies in different bins of X-ray luminosity. The thin vertical line separates Classes 1 and 2, which show MIR evidence of an AGN, from other classes, which show only star formation features in the MIR. X-ray luminosities are from 2 to 10 keV; see note to Table 5.

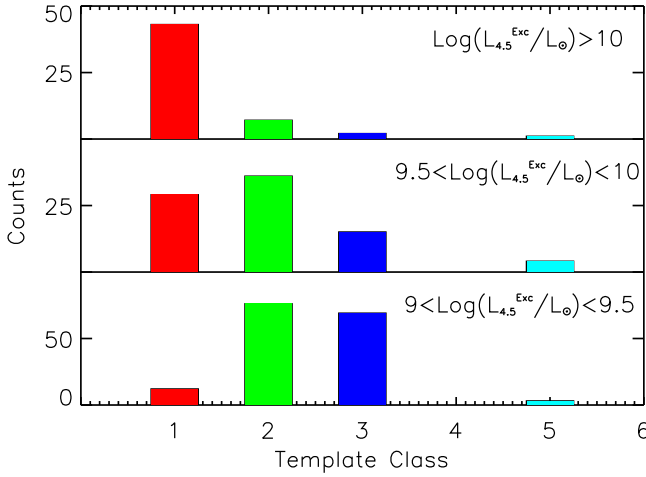


Figure 20. Histograms showing SED classes for galaxies with excess $4.5 \mu\text{m}$ luminosity as defined by Equation (3). Rows show galaxies in different bins of $L_{4.5}^{\text{Exc}}$.

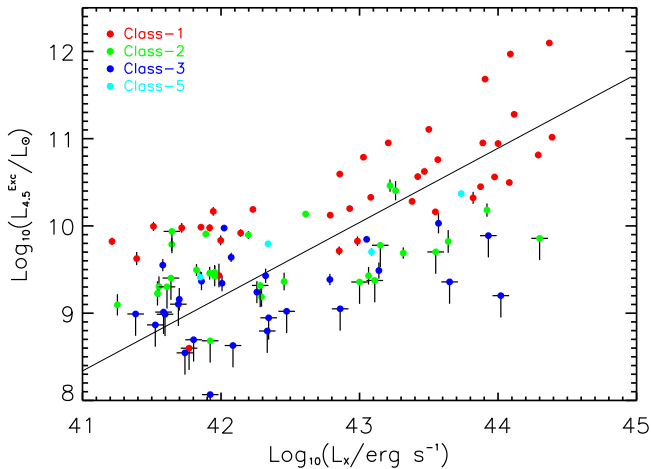


Figure 21. Excess $4.5 \mu\text{m}$ luminosity (Equation (3)) as a function of X-ray luminosity. Points are color-coded by template class as shown in the legend. The line shows the best linear fit to the data (Equation (4)).

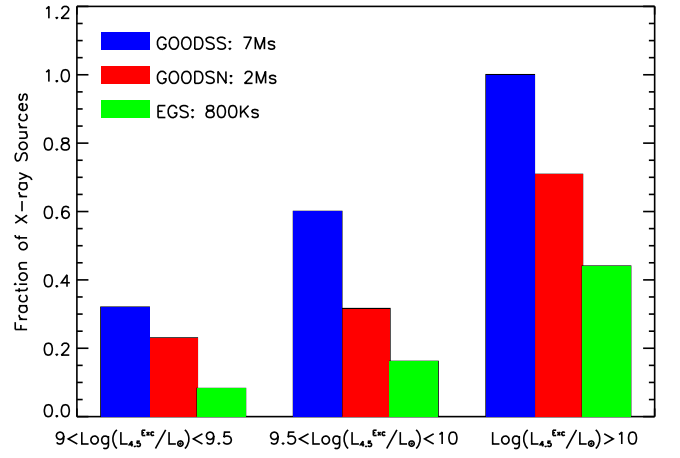


Figure 22. Histograms of X-ray-detected fraction of sources with $4.5 \mu\text{m}$ luminosity excess. Colors show different fields, which have differing depths of X-ray observation as indicated in the legend. Three sets show different bins of $L_{4.5}^{\text{Exc}}$ (Equation (3)).

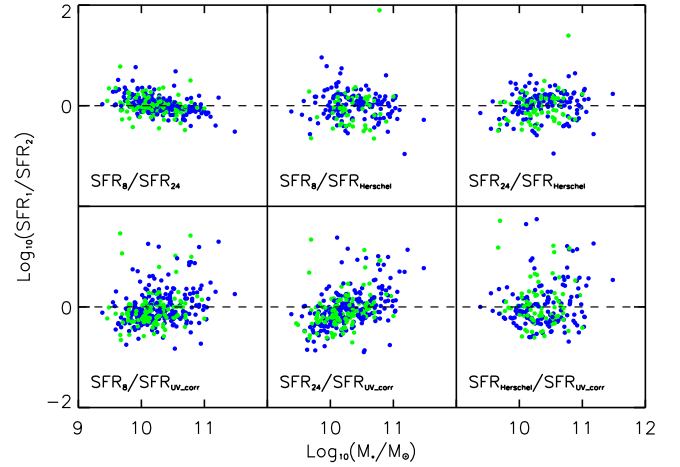


Figure 23. Comparison of SFR estimators as a function of stellar mass. Text in each panel identifies the ratio plotted. Only galaxies with Class 2 (green points) and Class 3 (blue points) SEDs, which should be relatively unaffected by AGNs, are shown. Galaxies with significant $L_{4.5}^{\text{Exc}}$ are omitted for the same reason. Horizontal dashed lines show equality.

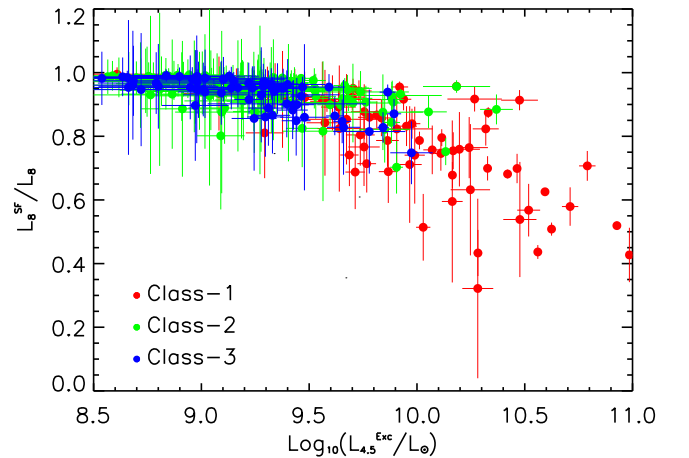


Figure 24. Fraction of star formation luminosity in L_8 as a function of AGN luminosity as measured by $L_{4.5}^{\text{Exc}}$. Points are color-coded by SED type. Most galaxies with $L_{4.5}^{\text{Exc}} > 10^{9.5}$ have median $L_8^{\text{SF}}/L_8 = 0.85$, implying that L_8 is usually a good measure of SFR.

FIR luminosity, L_{FIR} , being less affected by the AGN emission (Dai et al. 2018), should however still be a valid SFR measure. All but 6 of the 20 galaxies have enough FIR detections to give SFR. Figure 16 shows SEDs for five examples with at least three Herschel detections. Their L_{IR} qualifies them as LIRGs. The overall picture confirms the correlation between L_8 and SFR for all galaxies (Elbaz et al. 2011), including AGNs at $z \sim 1$. Our study refines the SFR estimates and allows us to study the relation between star formation and AGN (Section 4.3).

4.3. Coevolution of Galaxies and Central SMBHs

Galaxy mass assembly is correlated with central SMBH growth. This is supported by the observed correlation between the galaxy-bulge stellar mass and central SMBH mass (e.g., Magorrian et al. 1998; Kormendy & Ho 2013). This coevolution scenario implies a correlation between SFR and the SMBH's accretion rate as calculated from L_{AGN} (e.g., Netzer 2009; Rosario et al. 2013; Dai et al. 2018; Yang et al. 2019). Several studies found that AGNs, especially with $L_X > 10^{44}$ erg s $^{-1}$, show a good correlation between SFR and L_{AGN} (e.g., Lutz et al. 2010; Rosario et al. 2012; Chen et al. 2013, 2015; Hickox et al. 2014; Azadi et al. 2015; Xu et al. 2015; Dai et al. 2018; Yang et al. 2019).

Practical estimates of the stellar mass for AGNs can be complicated. A strong AGN has significant emission in both the visible and NIR bands, and this emission must be subtracted when estimating host-galaxy stellar mass. Stellar masses for galaxies in the CANDELS fields were derived using SEDs (Mobasher et al. 2015). This method in principle fits and subtracts the AGN contribution but with some uncertainty. Most X-ray AGNs in this sample have large HI column densities, suggesting they are dust-obscured in visible light. According to Silva et al. (2004) and Aird et al. (2018), an AGN with $N_{\text{H}} > 10^{22}$ cm $^{-2}$ has a negligible contribution to its host SED in the visible bands. MIR-selected AGNs without X-ray detection are also likely to be dusty. The sample has only two AGNs with $L_X > 10^{44}$ erg and $N_{\text{H}} < 10^{22}$ cm $^{-2}$. Yet their stellar masses are already on the lower end, at $\log M_* = 10.14$ and $10.45 M_{\odot}$, respectively. It therefore seems unlikely that AGNs are causing large overestimates in stellar mass. Mobasher et al. (2015) estimated the uncertainties in their masses to be 0.16 dex, but uncertainties for strong AGNs will be larger.

Figure 25 shows that the AGN luminosity, $L_{4.5}^{\text{Exc}}$, is not correlated with host-galaxy stellar mass. (For this study, we have used $L_{4.5}^{\text{Exc}}$ instead of L_X as a proxy for AGN luminosity.) The Class 1 subsample (AGNs) has the lowest average stellar mass ($\log_{10} M_*/M_{\odot} = 10.16 \pm 0.59$ standard deviation), and objects with Class 3 SEDs (star-forming galaxies) have the highest average stellar mass ($\log_{10} M_*/M_{\odot} = 10.35 \pm 0.41$). Values for Class 2 are intermediate $\log_{10} M_*/M_{\odot} = 10.29 \pm 0.38$.

Figure 26 shows a positive but weak correlation between $L_{4.5}^{\text{Exc}}$ and SFR for objects with Class 1 SEDs (Spearman rank coefficient $r_s = 0.2$). Previous studies in this AGN luminosity range (Chen et al. 2013, 2015; Rosario et al. 2013; Hickox et al. 2014; Azadi et al. 2015; Xu et al. 2015; Dai et al. 2018) yielded a wide range of relations between AGN luminosity and SFR from almost linear to none. At a given $L_{4.5}^{\text{Exc}}$, objects with a Class 2 SED have a higher SFR than objects with a Class 1 SED. This is consistent with the definition of a Class 2 SED as

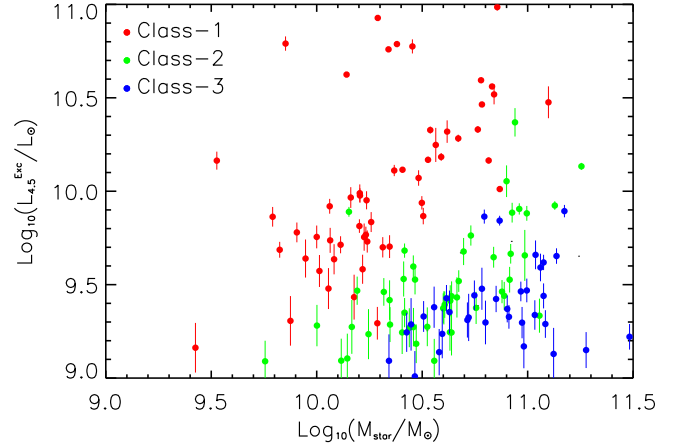


Figure 25. AGN luminosity vs. stellar mass. AGN luminosity is here measured by $L_{4.5}^{\text{Exc}}$, and only galaxies with at least 3σ significant values are shown. Points are color-coded by SED class as indicated in the legend.

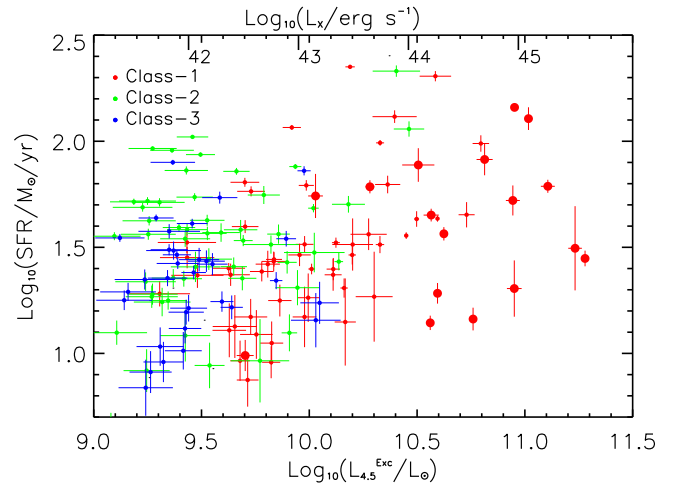


Figure 26. AGN luminosity vs. SFR. AGN luminosity is here measured by $L_{4.5}^{\text{Exc}}$, and only galaxies with at least 3σ significant values are shown. Points are color-coded by SED class as indicated in the legend. Large points indicate galaxies with low L_8^{SF}/L_8 whose SFRs were derived from their FIR luminosities. Other SFRs used in this plot were derived from L_8^{SFR} (Equation (A6)). The range on the abscissa is equivalent to $41 < \log_{10}(L_X/\text{erg s}^{-1}) < 44$ according to the $L_{4.5}^{\text{Exc}}-L_X$ correlation in Figure 21, and corresponding values of L_X are shown on the upper abscissa. The Spearman coefficient is 0.07 for all objects in this figure and about 0.2 for objects with Class 1 SEDs.

a composite one, consisting of both strong star formation and AGN features. There are 32 objects with significant $L_{4.5}^{\text{Exc}}$ and a Class 3 SED, but most are weak AGNs with $L_{4.5}^{\text{Exc}} \lesssim 10^{9.5} L_{\odot}$ and $L_X \lesssim 10^{42}$ erg s $^{-1}$.

Most galaxies at $z \approx 1$ have SFR correlated with their stellar mass; this is known as the main-sequence relation (Elbaz et al. 2011). When star formation is quenched, a galaxy drops off the main-sequence relation and becomes quiescent. Several models (e.g., Fabian 2012; Ishibashi & Fabian 2012; Alatalo et al. 2015; Man & Belli 2018; Chen et al. 2020) propose that an AGN is involved in quenching the star formation. Figure 27 shows the SFR relative to the main-sequence SFR at each galaxy's redshift. Most galaxies scatter around the main sequence regardless of their SED Class. This is further demonstrated in Figure 28, which shows that most galaxies, including those with AGNs, have SFR on the main sequence. Indeed, a majority of galaxies with $M_* > 10^{10.5} M_{\odot}$ and Class 1

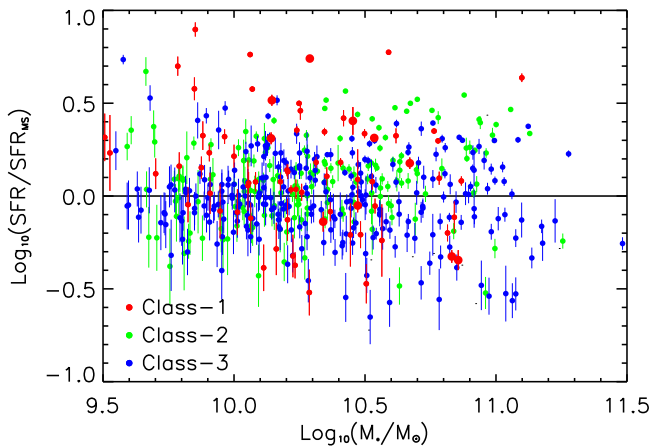


Figure 27. SFR relative to the galaxy main sequence for the $16\ \mu\text{m}$ selected galaxies. The main-sequence SFR as a function of M_* and redshift was from Lee et al. (2015). Points show galaxies color-coded by SED type as indicated in the legend, and the horizontal line marks the main sequence. Larger dots indicate the objects with strong AGN emission whose SFRs were derived from the FIR luminosity.

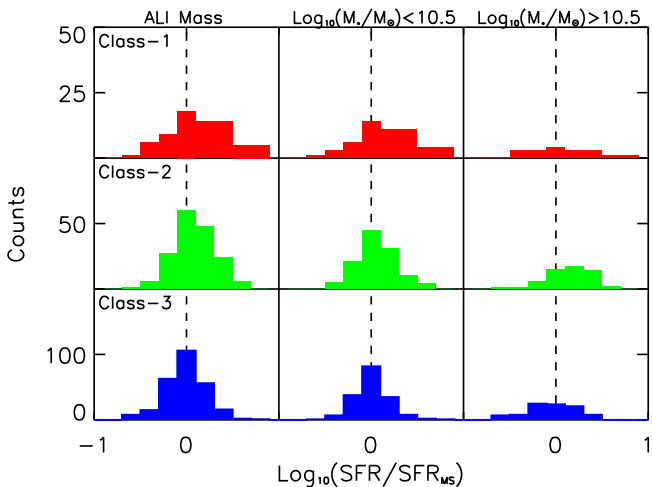


Figure 28. Histograms of SFR relative to the galaxy main sequence. Each row shows one SED class. The left column shows all objects in the respective excess condition (top row) or Class (other rows), and the middle and right columns show objects with low and high stellar mass as indicated.

or Class 2 SEDs have SFR above the main sequence despite all AGNs having a symmetric distribution around the main sequence. This is generally consistent with previous observations that X-ray-selected AGNs up to $z \sim 4$ are on the main sequence (e.g., Mullaney et al. 2015; Aird et al. 2019; Bernhard et al. 2019; Suh et al. 2019). Our sample does not include a substantial AGN population below the main sequence as found by some (Shimizu et al. 2015; Bain et al. 2020; Stemo et al. 2020) for local and for distant but $z < 4$ AGNs. Presumably, this is a result of our rest $\sim 8\ \mu\text{m}$ sample selection. The SED class of each AGN host in our sample is mainly controlled by AGN luminosity. Galaxies with higher AGN luminosities tend to fall into Class 1 because the AGN overwhelms star formation signatures. The overall tendency of galaxies in all classes to follow the main-sequence relation suggests that AGN luminosity and SFR change in tandem.

Galaxies in our sample show no reduction in SFR when an AGN is present, as one might expect in an AGN-quenching scenario (Fabian 2012; Ishibashi & Fabian 2012; Alatalo et al. 2015; Man & Belli 2018). Figure 28 shows that galaxies with an AGN component show a similar SFR/SFR_{MS} distribution to that of star-forming galaxies. Indeed an AGN component could exist in most galaxies in our sample, though it would be veiled in the ones with a higher SFR. On the other hand, galaxies with Class 1 SEDs, along with high-mass galaxies having Class 2 SEDs, tend to lie above the main sequence. This implies, if anything, enhanced star formation in AGN-dominated galaxies. To further test this, Figure 29 tracks how SFRs are affected by AGNs in each mass bin. Class 1 SEDs become rarer as stellar masses increase, consistent with the increasing dominance of the star formation component in massive galaxies. In addition, very few AGNs with $\log_{10}(L_{4.5}^{\text{Exc}}/L_{\odot}) > 10$ have SFR below the main-sequence value. This is particularly noticeable for AGNs in the $10.5 < \log_{10}(M_*/M_{\odot}) < 11$ bin. One interpretation of Figure 29 is that AGN luminosity decreases when its host galaxy evolves across the main-sequence line. In the highest-mass $\log_{10}(M_*/M_{\odot}) > 11$ bin, all AGNs have lower $L_{4.5}^{\text{Exc}}$, and only three of them are above the main sequence. The implication on the distribution of AGNs along the main sequence is twofold: (1) AGN accretion increases together with star formation activity; (2) whatever quenches the star formation may also quench its central AGN accretion. Given the very different timescales involved, it is difficult to draw conclusions about AGN feedback as a quenching mechanism from the comparison of AGN emission and IR SFRs in our sample, but the parallel decline in AGN accretion rate and SFR seen here is consistent with the so-called halo-quenching models, in which halo gas cooling becomes less effective as halo mass increases (e.g., Correa et al. 2018). The decline in global cool-gas inflow thus deprives both the galaxy and the black hole of further fuel to grow.

5. Summary

A sample of 705 $16\ \mu\text{m}$ selected, $0.8 < z < 1.3$ galaxies mostly have $11 < \log_{10}(L_{\text{IR}}/L_{\odot}) < 12$, qualifying them as LIRGs. In most cases, their rest-frame $1.6\ \mu\text{m} < \lambda < 12\ \mu\text{m}$ SEDs are well fit by local-galaxy SED templates. Most galaxies in the sample follow the galaxy main-sequence relation between stellar mass and SFR. Their $8\ \mu\text{m}$ luminosity function shows a strong evolution from $z \sim 0$ corresponding to the strong SFRD evolution over that redshift range.

Based on fitting the MIR SEDs, 84% of the galaxies in our $16\ \mu\text{m}$ sample are star-forming—best fit by either star-forming or composite templates. While all of these are likely to show PAH emission and be forming stars, about 17% of the Class 2 +3 galaxies show an AGN component revealed by either $4.5\ \mu\text{m}$ luminosity exceeding that from stellar processes (stellar photospheres plus dust heated by star formation) or X-ray luminosity exceeding $10^{42}\ \text{erg s}^{-1}$. About 15% of the sample are best fit by an AGN template. No object in our sample can be fit by a quiescent galaxy template, not surprising given the $16\ \mu\text{m}$ selection. Nine objects (1.3%) show neither PAH emission nor strong rest- $4.5\ \mu\text{m}$ continuum. All of these objects have $M_* > 10^{10}\ M_{\odot}$ although the local templates that fit their SEDs have $M_* < 10^9\ M_{\odot}$. Further investigation is needed for these special objects.

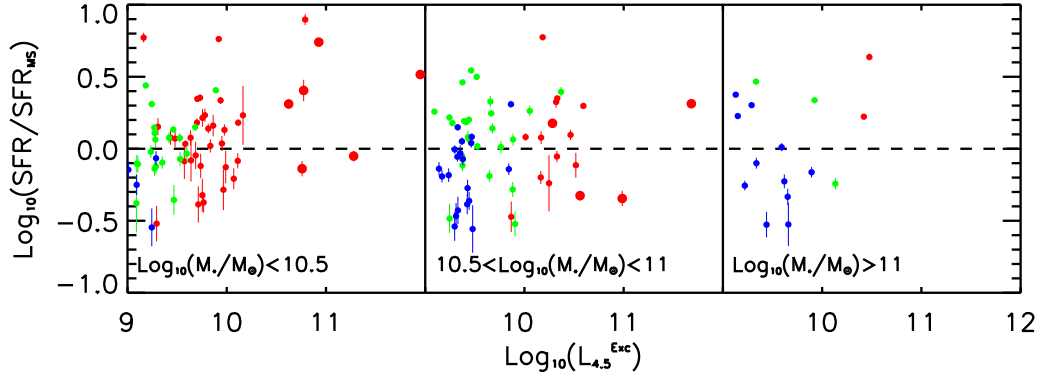


Figure 29. SFR relative to the galaxy main sequence vs. AGN luminosity. AGN luminosity is here measured by $L_{4.5}^{\text{Exc}}$, and only galaxies with at least 3σ significant values are shown. Points are color-coded by SED type: red for Class 1, green for Class 2, and blue for Class 3. Panels show three bins of stellar mass as labeled.

Our fitting of galaxy SEDs for the sample permits accurate separation of MIR luminosities contributed by star formation and an AGN component. This is because the $L_{4.5}/L_{1.6}$ and $L_8/L_{1.6}$ color–color diagram shows a close correlation for star-forming galaxies, but galaxies with an AGN show excess emission at $4.5\ \mu\text{m}$ ($L_{4.5}^{\text{Exc}}$). This excess correlates well with X-ray luminosities for galaxies having Chandra X-ray detections, and $L_{4.5}^{\text{Exc}}$ should therefore be a useful AGN luminosity indicator, as it is for local galaxies. As for SFR indicators, SFRs estimated from $8\ \mu\text{m}$ luminosity (L_8), $24\ \mu\text{m}$ flux density, FIR luminosity, and UV-corrected flux yield consistent results for this sample of LIRGs. SFRs derived from L_8 and $24\ \mu\text{m}$ flux density have the lowest scatter. Therefore, we suggest that L_8 can trace the SFR as accurately as the $24\ \mu\text{m}$ flux density for this LIRG sample and more accurately than SFR derived from UV flux.

Our sample galaxies show a correlation between AGN luminosity (as measured by $L_{4.5}^{\text{Exc}}$) and SFR, indicating a coevolution between black hole accretion rate and star formation. Also, galaxies with high AGN luminosities and an SED showing a dominant AGN tend to lie above the star formation main sequence. These galaxies are seen predominantly at low stellar mass and are absent at $M_* > 10^{11} M_\odot$. AGN accretion therefore appears to shut down along with star formation when enough stellar mass has been accumulated. Although galaxies with and without an AGN follow the main sequence, we cannot rule out the possibility of AGN-related quenching. Nevertheless, the positive correlation between AGN and SFR and the lack of AGNs at the massive end tends to favor the halo-mass quenching mechanism, which stops not only galaxy-wide star formation but also gas feeding the accretion of the central massive black hole.

This work is based in part on observations made with the Spitzer Space Telescope, which is operated by the Jet Propulsion Laboratory, California Institute of Technology under a contract with NASA. Support for this work was provided by the Chinese National Nature Science Foundation grant No. 10878003. This work was supported in part by the National Key R&D Program of China via grant No. 2017YFA0402703 and by NSFC grants 11433003, 11822303, 11773020, 11733002, 11933003, 11373034, 11803044, and 11673028. Additional support came from the Chinese Academy of Sciences (CAS) through a grant to the South America Center for Astronomy (CASSACA) in

Santiago, Chile. G.M. acknowledges the Villum Fonden research grant 13160 “Gas to stars, stars to dust: tracing star formation across cosmic time” and the Cosmic Dawn Center of Excellence funded by the Danish National Research Foundation under grant No. 140. D.R. acknowledges support from STFC through grant No. ST.S000488.1.

Facilities: Spitzer (IRAC), Spitzer (MIPS), Spitzer (IRS), Keck, Subaru.

Appendix

Measured broadband (rest-frame) luminosities L_8 and $L_{4.5}$ can be considered as the sum of star-forming and AGN components:

$$L_8 = L_8^{\text{SFR}} + L_8^{\text{Exc}}, \quad (\text{A1})$$

and

$$L_{4.5} = L_{4.5}^{\text{SFR}} + L_{4.5}^{\text{Exc}}. \quad (\text{A2})$$

Here, $L_{4.5}^{\text{SFR}}$ and L_8^{SFR} consist of both photospheric emission from stars and dust emission from star formation regions, and $L_{4.5}^{\text{Exc}}$ is taken to be AGN luminosity. For both $L_{4.5}^{\text{SFR}}$ and L_8^{SFR} , we adopt the relation found in Figure 10, and we assume that $L_{1.6}$ is only from stellar photospheres:

$$L_{4.5}^{\text{SFR}} = (L_8^{\text{SFR}} + 0.93L_{1.6})/11.8. \quad (\text{A3})$$

The AGN intrinsic SED model from Mullaney et al. (2011) gives a power law $\lambda F_\lambda \propto \lambda^\alpha$ with $-0.3 < \alpha < 0.8$ for the AGN component. This gives

$$L_8^{\text{Exc}}/L_{4.5}^{\text{Exc}} = (8/4.5)^\alpha. \quad (\text{A4})$$

By solving the above three equations, we reach

$$L_{4.5}^{\text{Exc}} = \epsilon(11.8L_{4.5} - L_8 + 0.93L_{1.6}), \quad (\text{A5})$$














where $\epsilon = [11.8 - (8/4.5)^\alpha]^{-1}$, a weak function of α . For the expected $\alpha \approx 0$, $\epsilon \approx 0.093$. ($\epsilon = 0.091\text{--}0.098$ for the range of α above.) The star-forming component in L_8 is then

$$L_8^{\text{SFR}} = L_8 - L_{4.5}^{\text{Exc}}(8/4.5)^\alpha. \quad (\text{A6})$$

Qualitatively, L_8 measures SFR with a modest AGN correction while $L_{4.5}$ measures the AGN with a modest star formation correction. For this LIRG sample, photospheric emission at rest $8\ \mu\text{m}$ is only 2%–3% of L_8^{SFR} . We therefore need not subtract photospheric emission from L_8 when calculating the SFR, and

the relatively small coefficient on $L_{1.6}$ shows that any AGN contribution at $1.6 \mu\text{m}$ will make little difference. Error bars, including uncertainties in the parameters, for L_8^{SFR} and $L_{4.5}^{\text{Exc}}$ were propagated according to the above equations.

ORCID iDs

J.-S. Huang  <https://orcid.org/0000-0001-6511-8745>
 Y.-S. Dai (戴昱)  <https://orcid.org/0000-0002-7928-416X>
 S. P. Willner  <https://orcid.org/0000-0002-9895-5758>
 S. M. Faber  <https://orcid.org/0000-0003-4996-214X>
 C. Cheng  <https://orcid.org/0000-0003-0202-0534>
 H. Yan  <https://orcid.org/0000-0001-7592-7714>
 D. Rigopoulou  <https://orcid.org/0000-0001-6854-7545>
 M. Pereira Santaella  <https://orcid.org/0000-0002-4005-9619>
 G. Magdis  <https://orcid.org/0000-0002-4872-2294>
 I. Cortzen  <https://orcid.org/0000-0001-9197-7623>
 G. G. Fazio  <https://orcid.org/0000-0002-0670-0708>
 L. Fan  <https://orcid.org/0000-0003-4200-4432>
 G. Jin  <https://orcid.org/0000-0003-3087-318X>
 A. Esamdin  <https://orcid.org/0000-0003-1845-4900>

References

- Aird, J., Coil, A. L., & Georgakakis, A. 2018, *MNRAS*, 474, 1225
 Aird, J., Coil, A. L., & Georgakakis, A. 2019, *MNRAS*, 484, 4360
 Alatalo, K., Lacy, M., Lanz, L., et al. 2015, *ApJ*, 798, 31
 Alonso-Herrero, A., Pereira-Santaella, M., Rieke, G. H., & Rigopoulou, D. 2012, *ApJ*, 744, 2
 Alonso-Herrero, A., Rieke, G. H., Rieke, M. J., et al. 2006, *ApJ*, 650, 835
 Assef, R. J., Kochanek, C. S., Brodwin, M., et al. 2008, *ApJ*, 676, 286
 Assef, R. J., Kochanek, C. S., Brodwin, M., et al. 2010, *ApJ*, 713, 970
 Azadi, M., Aird, J., Coil, A. L., et al. 2015, *ApJ*, 806, 187
 Bain, C., Sanders, D., McPartland, C., & Auge, C. 2020, AAS Meeting Abstracts, 52, 283.07
 Balestra, I., Mainieri, V., Popesso, P., et al. 2010, *A&A*, 512, A12
 Bell, E. F., McIntosh, D. H., Katz, N., & Weinberg, M. D. 2003, *ApJS*, 149, 289
 Bernhard, E., Grimmer, L. P., Mullaney, J. R., et al. 2019, *MNRAS*, 483, L52
 Borch, A., Meisenheimer, K., Bell, E. F., et al. 2006, *A&A*, 453, 869
 Boselli, A., Lequeux, J., & Gavazzi, G. 2004, *A&A*, 428, 409
 Brandl, B. R., Bernard-Salas, J., Spoon, H. W. W., et al. 2006, *ApJ*, 653, 1129
 Brown, M. J. I., Moustakas, J., Smith, J.-D. T., et al. 2014, *ApJS*, 212, 18
 Burgarella, D., Buat, V., Takeuchi, T. T., Wada, T., & Pearson, C. 2009, *PASJ*, 61, 177
 Calzetti, D., Kennicutt, R. C., Engelbracht, C. W., et al. 2007, *ApJ*, 666, 870
 Caputi, K. I., Lagache, G., Yan, L., et al. 2007, *ApJ*, 660, 97
 Carleton, N. P., Elvis, M., Fabbiano, G., et al. 1987, *ApJ*, 318, 595
 Chabrier, G. 2003, *PASP*, 115, 763
 Chary, R., & Elbaz, D. 2001, *ApJ*, 556, 562
 Chen, C.-T. J., Hickox, R. C., Alberts, S., et al. 2013, *ApJ*, 773, 3
 Chen, C.-T. J., Hickox, R. C., Alberts, S., et al. 2015, *ApJ*, 802, 50
 Chen, Z., Faber, S. M., Koo, D. C., et al. 2020, *ApJ*, 897, 102
 Correa, C. A., Schaye, J., Wyithe, J. S. B., et al. 2018, *MNRAS*, 473, 538
 Cortzen, I., Garrett, J., Magdis, G., et al. 2019, *MNRAS*, 482, 1618
 Crocker, A. F., Calzetti, D., Thilker, D. A., et al. 2013, *ApJ*, 762, 79
 Daddi, E., Elbaz, D., Walter, F., et al. 2010, *ApJL*, 714, L118
 Dahlen, T., Mobasher, B., Faber, S. M., et al. 2013, *ApJ*, 775, 93
 Dai, Y. S., Elvis, M., Bergeron, J., et al. 2014, *ApJ*, 791, 113
 Dai, Y. S., Wilkes, B. J., Bergeron, J., et al. 2018, *MNRAS*, 478, 4238
 Dale, D. A., Aniano, G., Engelbracht, C. W., et al. 2012, *ApJ*, 745, 95
 Dale, D. A., Cook, D. O., Roussel, H., et al. 2017, *ApJ*, 837, 90
 Davies, L. J. M., Lagos, C., Del, P., Katsianis, A., et al. 2019, *MNRAS*, 483, 1881
 Desai, V., Soifer, B. T., Dey, A., et al. 2009, *ApJ*, 700, 1190
 Driver, S. P., & Robotham, A. S. G. 2010, *MNRAS*, 407, 2131
 Elbaz, D., Cesarsky, C. J., Fadda, D., et al. 1999, *A&A*, 351, L37
 Elbaz, D., Dickinson, M., Hwang, H. S., et al. 2011, *A&A*, 533, A119
 Elbaz, D., Leiton, R., Nagar, N., et al. 2018, *A&A*, 616, A110
 Engelbracht, C. W., Gordon, K. D., Rieke, G. H., et al. 2005, *ApJL*, 628, L29
 Faber, S. M., Willmer, C. N. A., Wolf, C., et al. 2007, *ApJ*, 665, 265
 Fabian, A. C. 2012, *ARA&A*, 50, 455
 Fang, G., Huang, J.-S., Willner, S. P., et al. 2014, *ApJ*, 781, 63
 Fang, J. J., Faber, S. M., Koo, D. C., et al. 2018, *ApJ*, 858, 100
 Farrah, D., Lonsdale, C. J., Weedman, D. W., et al. 2008, *ApJ*, 677, 957
 Fiore, F., Puccetti, S., Brusa, M., et al. 2009, *ApJ*, 693, 447
 Fu, H., Yan, L., Scoville, N. Z., et al. 2010, *ApJ*, 722, 653
 Galliano, F., Madden, S. C., Jones, A. P., Wilson, C. D., & Bernard, J.-P. 2005, *A&A*, 434, 867
 Genzel, R., Lutz, D., Sturm, E., et al. 1998, *ApJ*, 498, 579
 Gilli, R., Comastri, A., & Hasinger, G. 2007, *A&A*, 463, 79
 Goto, T., Oi, N., Ohya, Y., et al. 2015, *MNRAS*, 452, 1684
 Grogin, N. A., Kocevski, D. D., Faber, S. M., et al. 2011, *ApJS*, 197, 35
 Gruppioni, C., Lari, C., Pozzi, F., et al. 2002, *MNRAS*, 335, 831
 Hao, C. N., Xia, X. Y., Mao, S., Wu, H., & Deng, Z. G. 2005a, *ApJ*, 625, 78
 Hao, C.-N., Xia, X.-Y., Shu-DeMao, K., Deng, Z.-G., & Wu, H. 2008, *ChJAA*, 8, 12
 Hao, L., Spoon, H. W. W., Sloan, G. C., et al. 2005b, *ApJL*, 625, L75
 Helou, G., Malhotra, S., Hollenbach, D. J., Dale, D. A., & Contursi, A. 2001, *ApJL*, 548, L73
 Hensley, B. S., & Draine, B. T. 2020, *ApJ*, 895, 38
 Hickox, R. C., & Alexander, D. M. 2018, *ARA&A*, 56, 625
 Hickox, R. C., Mullaney, J. R., Alexander, D. M., et al. 2014, *ApJ*, 782, 9
 Hickox, R. C., Myers, A. D., Brodwin, M., et al. 2011, *ApJ*, 731, 117
 Hogg, D. W., Tremonti, C. A., Blanton, M. R., et al. 2005, *ApJ*, 624, 162
 Hopkins, P. F., Richards, G. T., & Hernquist, L. 2007, *ApJ*, 654, 731
 Houck, J. R., Charmandaris, V., Brandl, B. R., et al. 2004, *ApJS*, 154, 211
 Huang, J.-S., Faber, S. M., Daddi, E., et al. 2009, *ApJ*, 700, 183
 Huang, J.-S., Faber, S. M., Willmer, C. N. A., et al. 2013, *ApJ*, 766, 21
 Huang, J.-S., Glazebrook, K., Cowie, L. L., & Tinney, C. 2003, *ApJ*, 584, 203
 Huang, J.-S., Rigopoulou, D., Papovich, C., et al. 2007, *ApJL*, 660, L69
 Hunt, L. K., Testi, L., Casasola, V., et al. 2014, *A&A*, 561, A49
 Imanishi, M., Dudley, C. C., & Maloney, P. R. 2001, *ApJL*, 558, L93
 Inami, H., Armus, L., Charmandaris, V., et al. 2013, *ApJ*, 777, 156
 Ishibashi, W., & Fabian, A. C. 2012, *MNRAS*, 427, 2998
 Kormendy, J., & Ho, L. C. 2013, *ARA&A*, 51, 511
 Kormendy, J., & Richstone, D. 1995, *ARA&A*, 33, 581
 Kozłowski, S., Kochanek, C. S., Ashby, M. L. N., et al. 2016, *ApJ*, 817, 119
 Lacy, M., Storrie-Lombardi, L. J., Sajina, A., et al. 2004, *ApJS*, 154, 166
 Lambrides, E. L., Chiaberge, M., Heckman, T., et al. 2020, *ApJ*, 897, 160
 Lanzuisi, G., Delvecchio, I., Berta, S., et al. 2017, *A&A*, 602, A123
 Lanzuisi, G., Piconcelli, E., Fiore, F., et al. 2009, *A&A*, 498, 67
 Lapi, A., Raimundo, S., Aversa, R., et al. 2014, *ApJ*, 782, 69
 Le Floc'h, E., Papovich, C., Dole, H., et al. 2005, *ApJ*, 632, 169
 Lee, N., Sanders, D. B., Casey, C. M., et al. 2015, *ApJ*, 801, 80
 Li, A., & Draine, B. T. 2002, *ApJ*, 572, 232
 Luo, B., Brandt, W. N., Xue, Y. Q., et al. 2017, *ApJS*, 228, 2
 Lutz, D., Mainieri, V., Rafferty, D., et al. 2010, *ApJ*, 712, 1287
 Lutz, D., Maiolino, R., Spoon, H. W. W., & Moorwood, A. F. M. 2004, *A&A*, 418, 465
 Lutz, D., Poglitsch, A., Altieri, B., et al. 2011, *A&A*, 532, A90
 Madau, P., & Dickinson, M. 2014, *ARA&A*, 52, 415
 Magdis, G. E., Elbaz, D., Hwang, H. S., et al. 2010a, *MNRAS*, 409, 22
 Magdis, G. E., Rigopoulou, D., Huang, J.-S., & Fazio, G. G. 2010b, *MNRAS*, 401, 1521
 Magorrian, J., Tremaine, S., Richstone, D., et al. 1998, *AJ*, 115, 2285
 Mahajan, S., Ashby, M. L. N., Willner, S. P., et al. 2019, *MNRAS*, 482, 560
 Man, A., & Belli, S. 2018, *NatAs*, 2, 695
 Matute, I., La Franca, F., Pozzi, F., et al. 2006, *A&A*, 451, 443
 McGaugh, S. S., & Schombert, J. M. 2014, *AJ*, 148, 77
 Mobasher, B., Dahlen, T., Ferguson, H. C., et al. 2015, *ApJ*, 808, 101
 Moorwood, A. F. M. 1986, *A&A*, 166, 4
 Moster, B. P., Somerville, R. S., Newman, J. A., & Rix, H.-W. 2011, *ApJ*, 731, 113
 Mullaney, J. R., Alexander, D. M., Aird, J., et al. 2015, *MNRAS*, 453, L83
 Mullaney, J. R., Alexander, D. M., Goulding, A. D., & Hickox, R. C. 2011, *MNRAS*, 414, 1082
 Nandra, K., Laird, E. S., Aird, J. A., et al. 2015, *ApJS*, 220, 10
 Netzer, H. 2009, *MNRAS*, 399, 1907
 Newman, J. A., Cooper, M. C., Davis, M., et al. 2013, *ApJS*, 208, 5
 Oliver, S. J., Bock, J., Altieri, B., et al. 2012, *MNRAS*, 424, 1614
 Pahre, M. A., Ashby, M. L. N., Fazio, G. G., & Willner, S. P. 2004, *ApJS*, 154, 235
 Pearson, C. P., Oyabu, S., Wada, T., et al. 2010, *A&A*, 514, A8
 Peeters, E., Allamandola, L. J., Bauschlicher, C. W., et al. 2004, *ApJ*, 604, 252
 Pety, J., Teyssier, D., Fossé, D., et al. 2005, *A&A*, 435, 885

- Polletta, M., Tajer, M., Maraschi, L., et al. 2007, *ApJ*, 663, 81
- Rieke, G. H., Alonso-Herrero, A., Weiner, B. J., et al. 2009, *ApJ*, 692, 556
- Rigopoulou, D., Mainieri, V., Almaini, O., et al. 2009, *MNRAS*, 400, 1199
- Rigopoulou, D., Spoon, H. W. W., Genzel, R., et al. 1999, *AJ*, 118, 2625
- Roche, P. F., Aitken, D. K., Smith, C. H., & Ward, M. J. 1991, *MNRAS*, 248, 606
- Rodighiero, G., Lari, C., Fadda, D., et al. 2004, *A&A*, 427, 773
- Rosario, D. J., Santini, P., Lutz, D., et al. 2012, *A&A*, 545, A45
- Rosario, D. J., Santini, P., Lutz, D., et al. 2013, *ApJ*, 771, 63
- Rosenberg, J. L., Ashby, M. L. N., Salzer, J. J., & Huang, J.-S. 2006, *ApJ*, 636, 742
- Shimizu, T. T., Mushotzky, R. F., Meléndez, M., Koss, M., & Rosario, D. J. 2015, *MNRAS*, 452, 1841
- Silva, L., Maiolino, R., & Granato, G. L. 2004, *MNRAS*, 355, 973
- Silverman, J. D., Green, P. J., Barkhouse, W. A., et al. 2008, *ApJ*, 679, 118
- Spoon, H. W. W., Marshall, J. A., Houck, J. R., et al. 2007, *ApJL*, 654, L49
- Stemo, A., Comerford, J. M., Barrows, R. S., et al. 2020, *ApJ*, 888, 78
- Stern, D. 2015, *ApJ*, 807, 129
- Stern, D., Eisenhardt, P., Gorjian, V., et al. 2005, *ApJ*, 631, 163
- Suh, H., Civano, F., Hasinger, G., et al. 2019, *ApJ*, 872, 168
- Teplitz, H. I., Chary, R., Elbaz, D., et al. 2011, *AJ*, 141, 1
- Treyer, M., Schiminovich, D., Johnson, B. D., et al. 2010, *ApJ*, 719, 1191
- Valencic, L. A., & Smith, R. K. 2015, *ApJ*, 809, 66
- Wada, T., Oyabu, S., Ita, Y., et al. 2007, *PASJ*, 59, S515
- Wang, T., Elbaz, D., Alexander, D. M., et al. 2017, *A&A*, 601, A63
- Ward, M., Elvis, M., Fabbiano, G., et al. 1987, *ApJ*, 315, 74
- Wirth, G. D., Willmer, C. N. A., Amico, P., et al. 2004, *AJ*, 127, 3121
- Wu, H., Cao, C., Hao, C.-N., et al. 2005, *ApJL*, 632, L79
- Wu, Y., Charmandaris, V., Houck, J. R., et al. 2008, *ApJ*, 676, 970
- Xu, L., Rieke, G. H., Egami, E., et al. 2015, *ApJ*, 808, 159
- Xue, Y. Q., Luo, B., Brandt, W. N., et al. 2016, *ApJS*, 224, 15
- Yang, G., Brandt, W. N., Alexander, D. M., et al. 2019, *MNRAS*, 485, 3721